NUMERICAL AND EXPERIMENTAL INVESTIGATION OF TUBEAXIAL FAN NOISE

A THESIS SUBMITTED TO
THE GRADUATE SCHOOL OF NATURAL AND APPLIED SCIENCES
OF
MIDDLE EAST TECHNICAL UNIVERSITY

BY

AHMET BODUR

IN PARTIAL FULFILLMENT OF THE REQUIREMENTS
FOR
THE DEGREE OF MASTER OF SCIENCE
IN
MECHANICAL ENGINEERING

DECEMBER 2014

Approval of the thesis:

NUMERICAL AND EXPERIMENTAL INVESTIGATION OF TUBEAXIAL FAN NOISE

submitted by **AHMET BODUR** in partial fulfillment of the requirements for the degree of **Master of Science in Mechanical Engineering Department, Middle East Technical University** by,

Prof. Dr. Gülbin Dural Ünver
Dean, Graduate School of **Natural and Applied Sciences** _____

Prof. Dr. Tuna Balkan
Head of the Department, **Mechanical Engineering** _____

Prof. Dr. Mehmet Çalışkan
Supervisor, **Dept. of Mechanical Engineering** _____

Examining Committee Members:

Asst. Prof. Dr. Cüneyt Sert
Dept. of Mechanical Engineering, METU _____

Prof. Dr. Mehmet Çalışkan
Dept of Mechanical Engineering, METU _____

Asst. Prof. Dr. Yiğit Yazıcıoğlu
Dept of Mechanical Engineering, METU _____

Asst. Prof. Dr. Kıvanç Azgın
Dept of Mechanical Engineering, METU _____

Kamil Alper Yalçınkaya, M.Sc.
Expert Design Engineer, ASELSAN _____

Date: 5 December 2014

I hereby declare that all information in this document has been obtained and presented in accordance with academic rules and ethical conduct. I also declare that, as required by these rules and conduct, I have fully cited and referenced all material and results that are not original to this work.

Name, Last Name : Ahmet Bodur

Signature :

ABSTRACT

NUMERICAL AND EXPERIMENTAL INVESTIGATION OF TUBEAXIAL FAN NOISE

Bodur, Ahmet

M.Sc., Department of Mechanical Engineering

Supervisor: Prof. Dr. Mehmet Çalışkan

December 2014, 90 pages

In this study, the noise characteristic of a tube axial fan is investigated numerically and experimentally. The effects of blockage plate in front of the tube axial fan on the tube axial fan noise level are experimentally investigated. A computational aero-acoustic method is used to predict the flow induced fan noise. This method couples a flow solver and a wave equation solver. Unsteady flow analysis is performed with URANS (Unsteady Reynolds Average Navier Stokes Equation) method while acoustics radiation is computed with Ffowcs-Williams & Hawkings acoustics model in FLUENT. The numerical results is verified by a reasonably good agreement between numerical sound pressure level (SPL) of the tube axial fan in free-field and sound pressure level provided by acoustical measurement of the tube axial fan. The numerical and experimental studies give information about characteristics of the tube axial fan noise and about the effects of the blockage plate on fan noise level.

Keywords: Tube Axial Fan, Blockage Plate, Computational Fluid Dynamics, Computational Aero-Acoustics

ÖZ

TÜP EKSENEL FAN GÜRÜLTÜSÜNÜN SAYISAL VE DENEYSEL YÖNTEMLERLE ARAŞTIRILMASI

Bodur, Ahmet

Yüksek Lisans, Makina Mühendisliği Bölümü

Tez Yöneticisi: Prof. Dr. Mehmet Çalışkan

Aralık 2014, 90 sayfa

Bu çalışmada, tüp eksenel fan gürültüsü sayısal ve deneysel olarak ve blokaj plakasının tüp eksenel fan gürültüsüne etkisi deneysel olarak çalışılmıştır. Hava akışı kaynaklı gürültüleri tahmin etmek için hesaplamalı aero-akustik metodu kullanılmıştır. Yöntem akış çözücü ile dalga denklemi çözücüsünün bağlaşık kullanımından oluşmaktadır. Durağan olmayan akış analizi URANS (Unsteady Reynolds Average Navier Stokes Equation) yöntemiyle ve akustik yayılım analizi Ffowcs-Williams & Hawkings akustik modeliyle FLUENT kullanılarak yapılmıştır. Sayısal çalışmaların güvenirliği tüp eksenel fan için yapılan analiz değerlerinin tüp eksenel fanın kontrollü ses ölçümü ile elde edilen ses basıncı düzeyi değerleriyle uyumlu olması ile sağlanmıştır. Bu çalışmalar sonucunda tüp eksenel fan gürültüsü özellikleri ile ilgili sayısal ve deneysel bilgiler elde edilmiştir. Ayrıca, blokaj plakasının tüp eksenel fan gürültüsünü nasıl etkilediğine dair deneysel bilgiler irdelenmiştir.

Anahtar Kelimeler: Tüp eksenel fan, Soğutma Yüzgeçleri, Hesaplamalı Akışkan Dinamiği, Hesaplamalı Akış Akustiği

To My Youth

ACKNOWLEDGEMENTS

I would like to express literally the deepest of gratitude to my supervisor Prof. Dr. Mehmet Çalışkan for his guidance, advice, encouragement and support throughout the research.

I would also like to express my sincere thanks to Mr. Ali Karakuş, the Research Assistant in Mechanical Engineering department in METU, for his invaluable helps.

I would like to thank to Mr. Güvenç Canbaloğlu, Mechanical Engineer in ASELSAN, for his supports and helps.

I would also like to express my deepest thanks to Mr. K. Alper Yalçınkaya, Mechanical Engineer in ASELSAN, for his guidance and encouragements.

Furthermore, I would like to thank to my friends Mr. Bilgehan Yenice, Mr. Yusuf Dabakoğlu, Mr. Ferhat Aydoğan and Ms. Eylül Sucu for their supports, encouragements and patience during the long period of the study.

Finally and most importantly, I am grateful to my family for their support, love and encouragement throughout my life.

TABLE OF CONTENTS

LIST OF TABLES

LIST OF FIGURES

LIST OF SYMBOLS

ρ_i	density, density of i^{th} medium
t	Time
x_j	generalized coordinate, j^{th} generalized coordinate
u_j	velocity in j^{th} generalized coordinate
P_i	pressure at medium I
p	Acoustic pressure
P_0	Ambient pressure
∇	Gradient operator
λ	Wavelength of sound
c	Speed of sound
c_0	Bar velocity of sound
f	Frequency
L_p	Sound pressure level
L_W	Sound power level
P_{rms}	The rms of the acoustic pressure
P_{ref}	Reference sound pressure, 20 μPa
W_{rms}	The rms of the acoustic power
W_{ref}	Reference acoustic power, $10^{-12}\ Watt$
I	Acoustic intensity
ρ_0	Density of the acoustic medium

σ_{ij}	Viscous stress tensor
r	Distance, radial distance in spherical coordinates
e_{ij}	Rate of strain tensor
η	Shear coefficients of viscosity
η'	Bulk coefficients of viscosity
ω	Specific enthalpy
δ_{ij}	Kronecker delta
Ω	Angular velocity of the fan
κ	Thermal conductivity
ρ'	Density fluctuation
p'	Pressure fluctuation
u'	Velocity fluctuation
u_0	Mean flow velocity
u_{s_i}	Point velocity on the surface
θ	Angular position
k	Wave number
B	Number of blades
n	Harmonic number

ABBREVIATIONS

B&K	Brüel and Kjaer
BPF	Blade Passage Frequency
CAA	Computational Aero-Acoustics
CAD	Computer Aided Design
CFD	Computational Fluid Dynamics
DNS	Direct Numeric Simulation
FEM	Finite Element Method
FW-H	Ffowcs Williams & Hawkings
LES	Large Eddy Simulation
RANS	Reynolds Average Navier Stokes Equation
SPL	Sound Pressure Level
SWL	Sound Power Level
URANS	Unsteady Reynolds Average Navier Stokes Equation

CHAPTER 1

INTRODUCTION

1.1 General

Tube axial fan is one of the best choices in military applications for cooling systems such as electronic boxes, which include electronic cards. Temperature of the electronic cards should not exceed certain levels determined by the military standards. Therefore, the electronic cards should be continuously cooled. This is mostly achieved by tube axial fans owing to their high operational speeds accompanied by very high cooling performances with respect to other fan types. However, tube axial fan alone is not enough for cooling the system as required in military standards. Consequently, fins are designed on electronic boxes to amplify cooling performance of the system. Yet, another significant problem occurs while dealing with cooling of such systems; that is, the noise of the tube axial fan considerably increases when it is driven near fins of the electronic box.

In addition to the noise due to fan itself, fan interaction with an adjacent structure, which is a blockage plate in the present study, incredibly amplifies noise owing to the fact that flow passing through the fins and fan blades gives rise to fluctuating forces on fins and fan blades and thus generates higher noise. As a result, it is necessary that the unsteady forces on fins and fan blades be calculated in order to predict the tonal sound accurately. Then, thanks to an accurate prediction of the tonal noise, the effects of fin geometry or fan

geometry on the noise radiated can be obtained in order to comprehend flow-induced noise.

Unsteady forces in the turbulent flow should be solved accurately in order to predict the tonal noise and flow-induced noise, as well. As a result, a lot of attention must be given to the solution of the turbulent flow. Consequently, computational fluid dynamics (CFD) is employed to solve unsteady fluctuations and computational aero acoustics (CAA) is then applied together with CFD to obtain a good prediction of the tonal noise and flow-induced noise. As the flow is three-dimensional turbulent flow and wave equations are solved with turbulent equations, it requires a lot of time and computational power.

Noise due to the tube axial fan should be kept low to meet some requirements of military standards. Therefore, the noise of the tube axial fan and tube axial fan with adjacent structure are considered in this study.

1.2 Objective and Scope of the Thesis

In this study, the noise characteristic of a tube axial fan is investigated experimentally and theoretically. A computational fluid dynamics method (CFD) is used to solve the flow and computational aero-acoustic method (CAA) is applied to predict the flow induced fan noise. ANSYS FLUENT 14.0 is used for both CFD and CAA. In fact, FLUENT 14.0 couples a flow solver and a wave equation solver. Unsteady flow analysis is performed with URANS (Unsteady Reynolds Average Navier Stokes Equation) method while acoustics radiation is computed with Ffowcs Williams & Hawkings acoustics model in FLUENT 14.0. The theoretical results of the tube axial fan are checked with sound pressure level provided by acoustical measurement of the tube axial fan. Apart from tube axial fan alone, another case is studied experimentally. In other words, a blockage plate placed in front of the tube axial fan is investigated experimentally. These theoretical and experimental studies give information

about the noise characteristic of the tube axial fan and effects of the blockage plate on the noise radiated.

This study is divided into seven chapters. Following the introduction, Chapter 2 summarizes the surveyed literature relevant to the topic. In this chapter, some previous research works about axial fan noise is presented. Chapter 3 covers the theory of flow acoustics. In Chapter 4, numerical analysis is introduced. In this chapter, the flow model and acoustical model needed for FLUENT 14.0 are presented. Chapter 5 outlines the experimental set-up of sound pressure level measurement of the tube axial fan and the tube axial fan with blockage plate. In Chapter 6, results of the numerical and experimental studies are presented. In the last chapter, Chapter 7, the thesis is discussed and concluded. Also, some recommendations are expressed for future works.

CHAPTER 2

LITERATURE SURVEY

2.1 Experimental Studies

Hyrynen [3] carried out an experimental study to investigate the effects of the tip clearance and the effects of the impeller axial position in the inlet shroud. Vortices created by fluid passing through the tip clearance are liable to increase the noise level. As the blade clearance reduces, size of the vortices decreases as well. As a result, as the tip clearance is decreased, tip clearance induced noise is decreased in broadband levels. Moreover, the impeller axial position in the inlet shroud does not affect the radiated noise as much as tip clearance does.

Lin and Chou [4] studied the effect of the blockage plate placed in front of the axial fan on the noise of axial flow fans as shown in Figure 1. The effect of blockage plate on narrow band noise is negligible. Nevertheless, the presence of blockage plate increases broad band noise. In fact, the distance between fan and blockage plate is proportional to noise generated. Noise measurements are carried out in a semi-anechoic chamber. The microphone positions are illustrated in Figure 1.

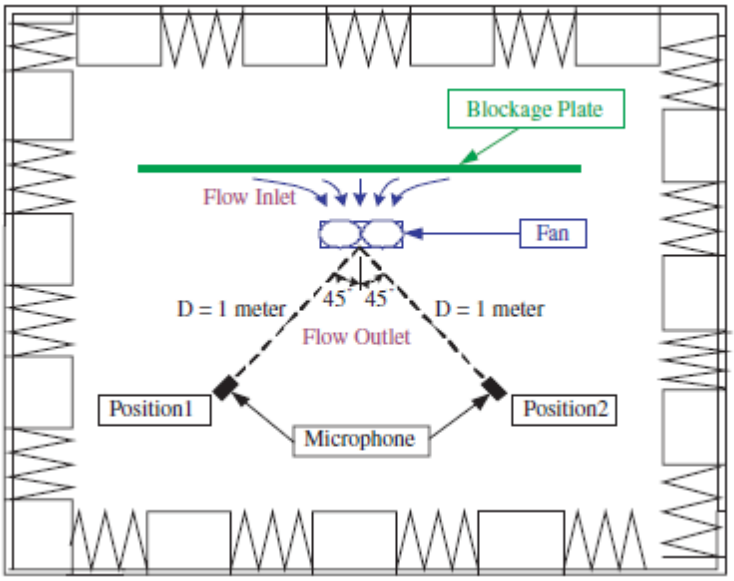

Figure 1 – Noise measurement set-up with microphone positions [4]

Cattanei, Ghio and Bongiovı [5] stated that reduction of the tonal noise can be achieved by using the uneven spacing rotor instead of evenly spaced rotor. Sound pressure level (SPL) measurements were performed in the Johnson Electric-GATE semi anechoic room. SPL was measured at three different angular locations at a distance of 1 m from the rotor center, that is, a microphone was placed upstream on the rotational axis, on the rotational plane and in the intermediate position. They concluded that evenly spaced rotor radiates more noise in discrete tones than unevenly spaced rotor does.

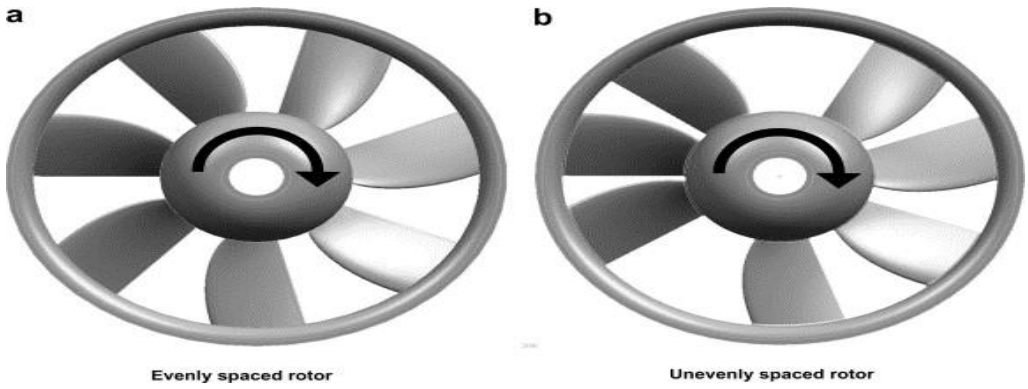

Figure 2 – Evenly spaced rotor and unevenly spaced rotor [5]

Shin, Bolton and Mongeau [6] put a thin metal foam in front of the axial fan as an inlet diffuser to improve inflow conditions of an axial fan. It is indicated that the inlet diffuser caused blade passing frequency tones to reduce, whereas it could give rise to higher harmonics and broadband noise to increase.

Figure 3 – An axial fan with an inlet diffuser [6]

Bianchi, Corsini and Sheard [7] investigated the effects of the tip end-plate geometries of axial fans on the axial fan noise in as much as the end-plate geometries influence the tip-leakage flow, vortex formation and swirl level. In other words, the aim of their investigation was to establish a cause-and-effect relationship between the tip flow dynamics and the radiated sound fields. They compared the aero acoustic performance of a datum blade with two proposed tip configurations. The sound measurements were carried out in the Fläkt Woods semi anechoic chamber in Colchester (UK). According to their experiments, the MVB tip configuration gave better results than the other two configurations in the broadband range. Moreover, they indicated that the datum and the TF fans have a characteristic of a dipolar-like emission, whereas the MVB fan has a monopole-like emission.

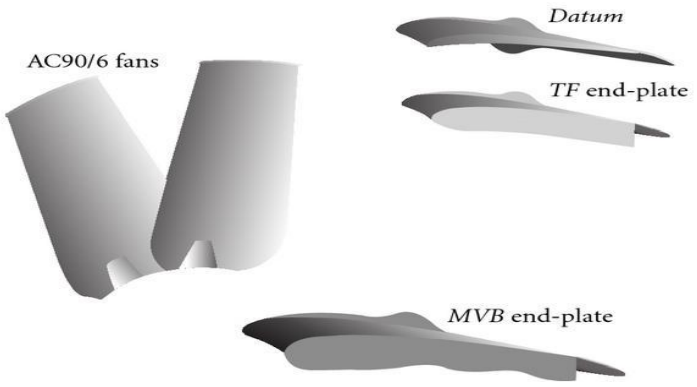

Figure 4 – Datum blade, TF end-plate (improved configuration) and MVB end-plate (a new tip appendage with variable thickness) [7].

2.2 Theoretical Studies

Kim, Jeon, and Cho [8] investigated the effects of pitch angle, sweep angle, maximum camber ratio and solidity on axial fan noise. SC/Tetra V5 and FlowNoise V2.1 are the software used for CFD computations and CAA computations, respectively. The flow is computed with the incompressible Navier-Stokes equations and Ffowcs-Williams and Hawkins equation with dipole source is used to determine aero acoustic pressure. It is concluded that the tip clearance between the blades and the bell mount stemmed from complex vortices. These vortices are amplified as the pressure gets higher. Unfortunately, complex vortices causes more noise at low flow rates.

Zhang and Jin [9] investigated the effects of blade-number induced noise in broadband level. They studied six different axial fans with different blade numbers (5,7,9,11,13,15) as shown in Figure 5.

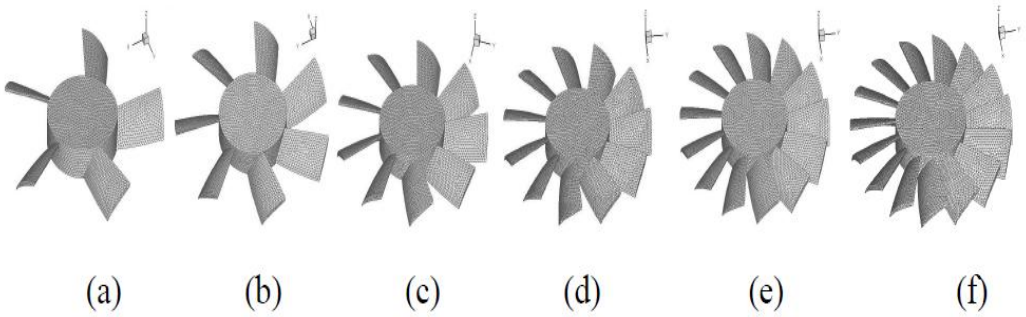

Figure 5 – Six different axial fans with different numbers [9].

Steady flow is calculated by employing the Standard k-ε viscous model and the SIMPLE algorithm is applied to couple pressure and velocity. The unsteady flow and noise are computed by using Large Eddy Simulation (LES) turbulent model with the Ffowcs – William Hawkings equation acoustics model. It is concluded that as the blade number increases from 5 to 11, broadband noise reduces; however, there is an increase in broadband noise as blade number rises from 11 to 15.

Ren, Heo, Kim and Cheong [10] optimized the shroud of an axial cooling fan for the generated noise. Response Surface Method is used with computational fluid dynamics. The flow is computed in the commercial CFD program ANSYS FLUENT. For the steady-state flows, rotating reference frame and RNG k-epsilon turbulent model are used. They found that the orifice length of the shroud and the serrated structure affect significantly the radiated noise. The shroud with serrated structure causes noise reduction. In addition, an increase in the length of orifice results in a rise in the flow rate. Therefore, speed of the axial fan can be reduced, which incredibly results in noise reduction.

Zhang and Jin [11] studied the distributions of broadband noise sources and the unsteady characteristics of vortex structure in small axial fan's internal flow field. Broad band noise model is used to determine the distribution of the broadband noise in the fan's internal flow field, whereas Large Eddy Simulation (LES) is applied to determine the unsteady vortex structure and FH-W is introduced to analyze aero dynamic noise due to the unsteady vortex structure. It is indicated that the

distribution of broadband noise sources are mainly at the tip clearance close to the blade trailing edge and one third of the chord length of blade trailing edge of small axial fans. The maximum sound power of broad band noise sources is greater at the tip clearance than at blade trailing edge. In fact, the tip leakage vortex and the trailing edge vortex shedding mainly affect broad band noise sources.

Pandian and Raj [12] investigated flow noise owing to unsteady flow past a circular cylinder. In the two-dimensional computational aero acoustic model, FW-H model is employed to calculate aero dynamic noise and is compared with broadband noise source model. It is indicated that dipole type source is the main noise source in an unsteady flow over cylinder due to the fluctuating pressure on the cylinder wall. Broadband noise model predicts the flow noise of an unsteady circular cylinder flows in a fully turbulent regime.

Sorgüven, Magagnato and Gabi [13] studied aero dynamic noise due to the flow around a circular cylinder and the flow noise around an airfoil in the wake of a cylinder. A high Reynolds number flow is calculated with LES and the sub-grid scale model used in LES is the adaptive k-τ model. The wall distance y^+ in the gird is kept equal or less than 1. On the other hand, FW-H model is used to solve the aero dynamic noise in the far field. LES gives better results in the case of the flow around a circular cylinder than the case of the flow around an airfoil in the wake of a cylinder.

2.3 Noise Generating Mechanism

Many researchers proved that axial fans have dipole characteristic of sound. Abom and Boden [14] experimentally, i.e. via measured two-port source data, demonstrated that the acoustical characteristic of an axial fan inside a duct is dipole. In fact, it is concluded that actual fan noise source can be replaced with an equivalent ideal dipole sound source in order to predict the induct noise radiation. Sorguven et al [15] indicated that dipolar sound source is dominant in axial fan noise at low Mach number and treated the axial fan noise source as a dipole sound

source neglecting monopole and quadrupole sound sources of the axial fan noise sources. It is shown that impellers are the main source of dipole noise. Gue et al. [16] recognized dipolar forces acting on the blades, vanes and casing, which are unsteady forces of solid surfaces, as the most significant contribution to the fan noise. Diaz et al. [17], in the numerical study, did not include the quadrupole source of the fan noise and experimentally proved that dipole is the dominant noise source. Tannoury et al. [18] acoustically considered the blade as compact and non-compact. In compact case, a single dipole is located at the blade center of gravity , whereas in the non-compact case, the blade consists of a set of compact dipoles. In compact case, it fails after the second harmonic of BPF. For higher order harmonics of BPF, the non-compact case is applied.

2.4 Directivity Pattern of an Axial Fan Noise

Bianchi, Corsini and Sheard determined experimentally the directivity pattern of a particular axial fan noise with different blade geometries shown in Figure 6. The rotor was rotated at a constant speed of 940 rpm. The noise was measured in far field at an angle of 30 degrees from the center line. Noise measurement locations are at several azimuthally locations from -90° to +90° from the rotor exhaust center line with an angular increment of 30°.

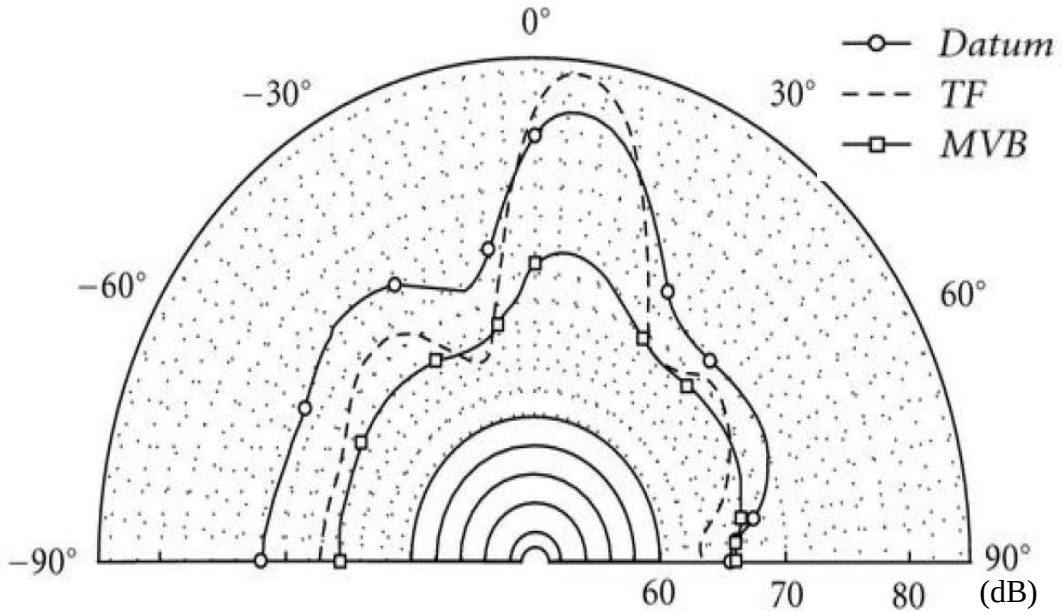

Figure 6 – Directivity of axial fan noise with different blade geometries [7]

Where the datum blade is typical of a class of low-noise industrial fans, TF is an improved configuration and MVB is a new tip appendage with variable thickness [7]. According to the Figure 6, while the datum and the TF fans have a characteristic of a dipolar-like emission, the MVB fan has a monopole-like emission.

Gue et al. [16] measured SPL of an axial fan in a semi-anechoic room. The axial fan noise was measured at five different positions. The microphones were placed at 1 m distance away from the fan with 45° increments azimuthally directions between inlet rotation axis of the fan and outlet rotation axis of the fan. The directivity of the axial fan with 3 blades having rotational speed of 1150 rpm is shown with theoretical results in Figure 7. The fan noise was numerically studied. A high Reynolds number k-ε turbulence model and FWH acoustic model were applied to solve flow and noise in commercial program CFD FLUENT, respectively. As a result, the axial fan is dipole as shown in Figure 7.

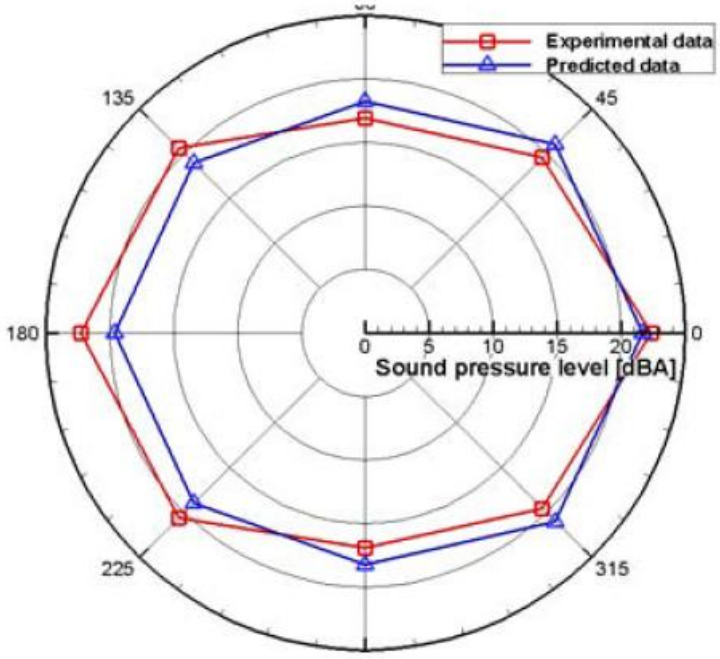

Figure 7 – Experimentally and predicted directivities of the axial fan [16]

Diaz et al. [17] recorded SPL of an axial fan at 5 m radial distance away from the axial fan with a 15° increments azimuthally directions. The axial fan has 9 rotors and 13 stator vanes. The directivity of the axial fan noise for BPF is shown in Figure 8. The inlet rotational axis of the fan was located at 0°. According to Figure 8, the axial fan has experimentally a characteristic of a dipole source and numerical result determines the characteristic of the axial fan as dipole source with 90° phase.

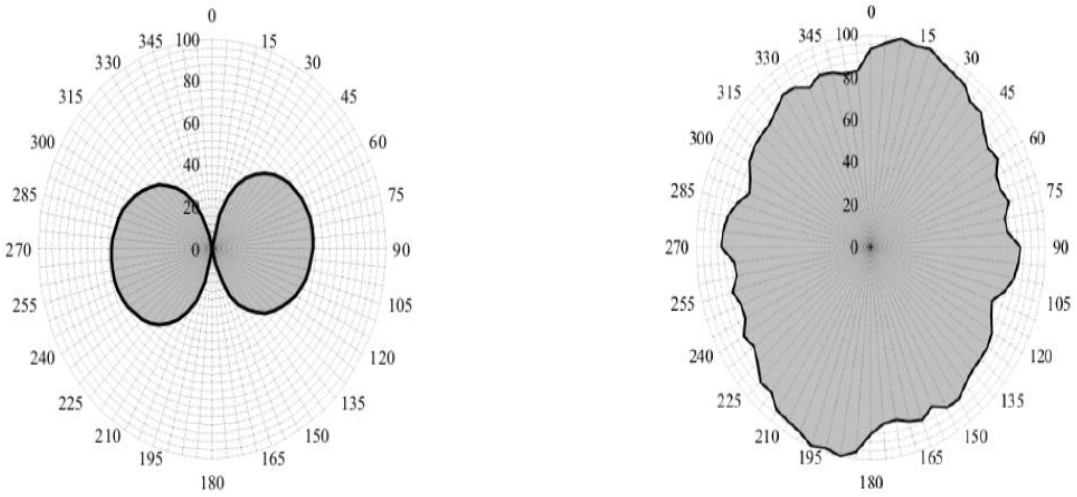

a) Numerical

b) Experimental

Figure 8 - Numerical and experimental directivities of the axial fan radiation at blade passage frequency (BPF) [17]

2.5 Fan Noise

Axial fan noise consists of two distinct components. These are broadband noise and discrete or tonal noise. Broadband noise is the noise spreading over a wide range of frequency, while discrete noise occurs at a certain frequency and at its harmonics. Fortunately, Neise [19] has classified aerodynamic noise of fan, and it's shown in Figure 9.

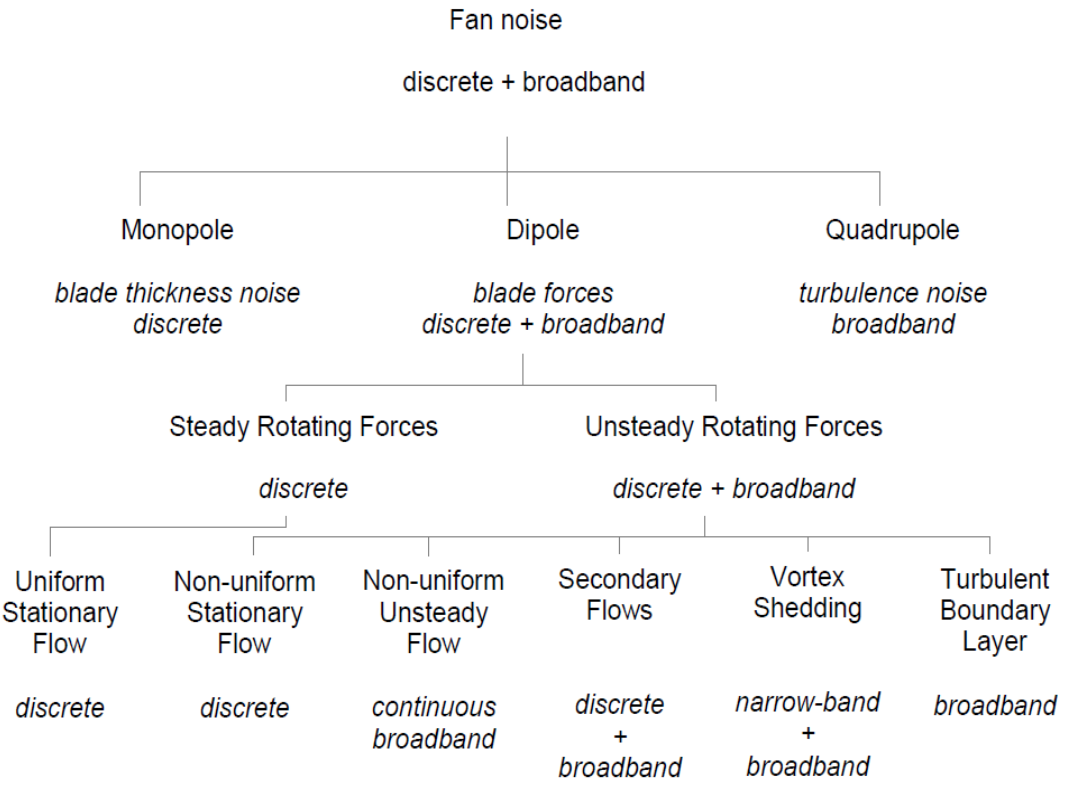

Figure 9 - Summary of aero acoustic fan noise generation mechanisms [19]

According to Figure 9, fan noise has three kinds of characteristic source of sound, namely, monopole, dipole and quadrupole. Monopole source, stemmed from the displacement of the fluid volume with the displacement of the blade of the fan. This kind of source mostly depends on the cross-section of the blade. In other words, efficiency of monopole source is proportional to the thickness of the blade. Hence, monopole source noise is called thickness noise and creates pure tones. At low Mach number and with thin blades, thickness noise loses its efficiency. Therefore, when fan speed is low and thickness of the blade is thin, this type of noise source can be discarded in the aero acoustic calculation of fan noise.

The other and the most significant characteristic noise source of fan noise is dipole. This kind of noise is referred as loading noise. Loading noise is stemmed from the steady rotating forces and unsteady rotating forces. At uniform stationary flow, steady rotating forces occur on the blade surfaces (lift and drag forces). These

forces give rise to noise radiation at a discrete frequency of blade passage frequency (BPF) and this noise is sometimes called Gutin noise. Periodic pressure oscillations occur on the blade surfaces and thus an observer in a fixed frame senses a periodic oscillation at BPF. This tonal noise becomes more effective than other types of fan noise at high speeds.

Blade Passage Frequency (BPF) $= \frac{B\Omega}{2\pi}$ and its harmonics are $f_n = \frac{nB\Omega}{2\pi}$

where B is the number of blades, Ω is the angular velocity of fan and n is the harmonicity index.

Non-uniform stationary flows are spatially non-uniform and time invariant flows. For instance, such flow occurs when fan operates near obstructions. In non-uniform flows, local lift and drag forces are caused periodically with time from the change of local velocities with circumferential position. As a consequence, these unsteady forces generate dipole sound at harmonics of BPF [20].

Noise due to vortex shedding is the most dominant broadband noise of dipole source. Since the velocity of the vortex shedding from fan blades varies with the radial distance, a broadband of shedding frequency occurs [21]. The pressure difference between the pressure side and suction side of the fan blade generates vortices. The most significant part of the vortices results from the trailing edge and tip of blades.

The interaction of the motion of the small-scale turbulence, which is quadropule, with boundary layers amplifies the weak noise of turbulence and this amplified noise radiates as dipole and is effective in broadband noise [21].

The quadropule source is generated from turbulence flow and radiates at broadband frequencies. This is called turbulence noise. This noise is not significant when Mach number does not exceed 0.8 [22].

According to the Figure 9, as the unsteady flow increases, there will be transition from discrete noise to the broadband noise. To put it differently, as the turbulent flow rises, broadband noise will be the dominant noise source.

CHAPTER 3

THEORY OF FLOW ACOUSTICS

3.1 Basic Principles and Terminology

3.1.1 Basic Acoustics

Sound is the sensation caused by small pressure perturbations that propagates through elastic media, while acoustics is the interdisciplinary science dealing with wave propagation in elastic media. A sound wave is described by speed of sound, wavelength and amplitude of sound wave. Speed of sound is related to temperature and the medium through which sound travels, whereas frequency does not affect the speed of sound. The wavelength is the distance traveled by a harmonic wave in one period. The wavelength can be expressed in terms of its frequency f and the speed of sound c as follows

$$\lambda = \frac{c}{f} \tag{1}$$

Sound pressure level (SPL) is determined in decibels as follows

$$L_p = 10 \log \left(\frac{p_{rms}}{p_{ref}} \right)^2 \text{ dB} \tag{2}$$

where p_{rms} is the rms of the acoustic pressure at a particular point and p_{ref} is the reference sound pressure whose value is 20 μPa. Sound pressure level depends on distance from the sound source, angular orientation and acoustical characteristics of the environment in which it is measured.

Sound power level (SWL) is calculated in decibels as follows

$$L_w = 10 \log\left(\frac{W_{rms}}{W_{ref}}\right) \text{ dB} \quad (3)$$

where W_{rms} is the rms of the acoustic power of a sound source and W_{ref} is the reference acoustic power whose value is 10^{-12} Watt. Acoustic power of a sound source does not depend on environment in which the source operates such as room, location, orientation and so on; on the other hand, it depends on operational characteristics of sound sources such as speed, loading so on and so forth.

Acoustic power can be written in terms of acoustic intensity I_{rms} as

$$W_{rms} = I_{rms} \times 4\pi r^2 \quad (4)$$

where acoustic intensity is expressed by

$$I_{rms} = \frac{p_{rms}^2}{\rho_0 c} \quad (5)$$

Here, ρ_0 is the density of the acoustic medium in which sound propagates.

3.1.2 Equations of Motion of a Fluid

3.1.2.1 Equation of Continuity

The rate of increase of the fluid mass within a fixed region of space V is equal to the net influx because of convection across the boundaries V. This can be expressed in terms of velocity u and fluid density ρ as follows

$$\frac{\partial \rho}{\partial t} + \nabla(\rho u) = 0 \tag{6}$$

or

$$\frac{1}{\rho}\frac{D\rho}{Dt} + \nabla u = 0 \tag{7}$$

where $\frac{D}{Dt} = \frac{\partial}{\partial t} + u\nabla \equiv \frac{\partial}{\partial t} + u_j \frac{\partial}{\partial x_j}$ is the material derivative and j = 1, 2, 3. When a fluid is incompressible, the equation of continuity becomes

$$\nabla u = 0 \tag{8}$$

3.1.2.2 Equation of Momentum

The momentum equation for a viscous fluid called the Navier – Stokes equation is the rate of change of momentum of a fluid particle. It can be expressed in terms of the pressure p, the viscous stress tensor σ_{ij}, and body forces (such as gravity) F per unit volume:

$$\rho \frac{Du_j}{Dt} = -\frac{\partial p}{\partial x_i} + \frac{\partial \sigma_{ij}}{\partial x_j} + F_i \equiv -\frac{\partial p_{ij}}{\partial x_j} + F_i \quad (9)$$

where

$$p_{ij} = p\delta_{ij} - \sigma_{ij} \quad (10)$$

is the compressive stress tensor. For an isotropic, Newtonian fluid (such as dry air and water)

$$\sigma_{ij} = 2\eta_{ij} + \left(\eta' - \frac{2}{3}\eta\right)\delta_{ij}e_{kk} \quad (11)$$

where

$$e_{ij} = \frac{1}{2}\left(\frac{\partial u_i}{\partial x_j} + \frac{\partial u_j}{\partial x_i}\right) \quad (12)$$

is the rate of strain tensor. η and η' are the shear and bulk coefficients of viscosity, respectively [23].

3.1.2.3 The Energy Equation

When specific entropy s is constant, flow motion can be determined with the equation of state derived from the continuity and momentum equations owing to the fact that constant specific entropy gives rise to a relation among thermodynamic variables.

However, since specific entropy is generally variable, an energy equation is necessary in order to achieve the conservation of total energy of the system. The energy equation can be written as

$$\rho \frac{D\omega}{Dt} - \frac{Dp}{Dt} \equiv \rho T \frac{Ds}{Dt} = \sigma_{ij} \frac{\partial v_i}{\partial x_j} - \frac{\partial Q_i}{\partial x_i} \tag{13}$$

where ω is specific enthalpy and $Q = -\kappa \nabla T$, where $\kappa > 0$ is the thermal conductivity [23].

3.2 Aerodynamic Sound

3.2.1 Lighthill's Acoustic Analogy

Lighthill was the first to introduce the theory of aerodynamic sound generated by a turbulent flow by reformulating the Navier-Stokes formula into an exact, inhomogeneous wave equation. Equations of motion of a compressible fluid – continuity and momentum equations – are expressed as by neglecting body forces (i.e. gravity):

Continuity Equation:

$$\frac{\partial \rho}{\partial t} + \frac{\partial (\rho u_i)}{\partial x_i} = 0 \tag{14}$$

Momentum Equation:

$$\frac{\partial (\rho u_i)}{\partial t} + \frac{\partial \left(\rho u_i u_j\right)}{\partial x_j} = -\frac{\partial p_{ij}}{\partial x_j} \tag{15}$$

Lighthill reformulated the Navier-Stokes formula by subtracting the space derivative of momentum equation from the time derivative of the continuity equation. As a result, he derived a wave equation as given

$$\frac{\partial^2 \rho}{\partial t^2} - \frac{\partial^2}{\partial x_i \, \partial x_j}\left(\rho u_i u_j\right) = \frac{\partial^2 p_{ij}}{\partial x_i \, \partial x_j} \tag{16}$$

Moreover, adding $-c_0^2 \frac{\partial^2 \rho}{\partial x_i^2}$ term to the both side of the Eqn. (16) and rearranging the equation gives

$$\frac{\partial^2 \rho}{\partial t^2} - c_0^2 \frac{\partial^2 \rho}{\partial x_i^2} = \frac{\partial^2}{\partial x_i \, \partial x_j}\left(\rho u_i u_j + (p - c_0^2 \rho)\delta_{ij} - \sigma_{ij}\right) \tag{17}$$

Eqn.(17) is the Lighthill's equation. Lighthill's equation is expressed by means of acoustic density fluctuation ρ' as follows:

$$\frac{\partial^2 \rho'}{\partial t^2} - c_0^2 \frac{\partial^2 \rho'}{\partial x_i^2} = \frac{\partial^2}{\partial x_i \, \partial x_j}\left(\rho u_i u_j + \left((p - p_0) - c_0^2(\rho - \rho_0)\right)\delta_{ij} - \sigma_{ij}\right) \tag{18}$$

where

$$p = p_0 + p' \qquad \rho = \rho_0 + \rho' \qquad u = u_0 + u'$$

In these equations, p_0 is the mean pressure, p' is the pressure fluctuations, ρ_0 is the mean density, ρ' is the density fluctuations, u_0 is the mean velocity and u' is the velocity fluctuations.

Eqn.(18) has no external forces. The Reynolds stress $\rho u_i u_j$ is the most dominant term and significant when the source region is rotational. $\left((p - p_0) - c_0^2(\rho - \rho_0)\right)$ term is the excess of momentum transfer and has the ideal fluid properties of

density and sound speed [23]. The viscous stress tensor σ_{ij} is usually neglected since it accounts for the attenuation of sound.

And Lighthill's tensor is:

$$T_{ij} = \rho u_i u_j + \left((p - p_0) - c_0^2(\rho - \rho_0)\right)\delta_{ij} - \sigma_{ij}$$

Thus, Lighthill's acoustic analogy, Eqn. (18), can be written in a more compact form as follows

$$\frac{\partial^2 \rho'}{\partial t^2} - c_0^2 \frac{\partial^2 \rho'}{\partial x_i^2} = \frac{\partial^2 T_{ij}}{\partial x_i \, \partial x_j} \tag{19}$$

T_{ij} is quadrupole sources. Consequently, aerodynamic sound generated in a stationary and ideal source region can be calculated by solving Eqn. (19).

3.2.2 The Ffowcs Williams-Hawkings Equation

Sound calculated by Lighthill's equation is solely due to quadrupole source. In fact, there are no solid bodies or motions in source region. As a result, in order to include the effects of solid bodies and motions in source region, Ffowcs Williams and Hawkings extended Lighthill's acoustic analogy to be able to account for the monopole and dipole sources on the solid body surfaces. FW-H converted real bodies into mathematical surfaces as shown in Figure 10.

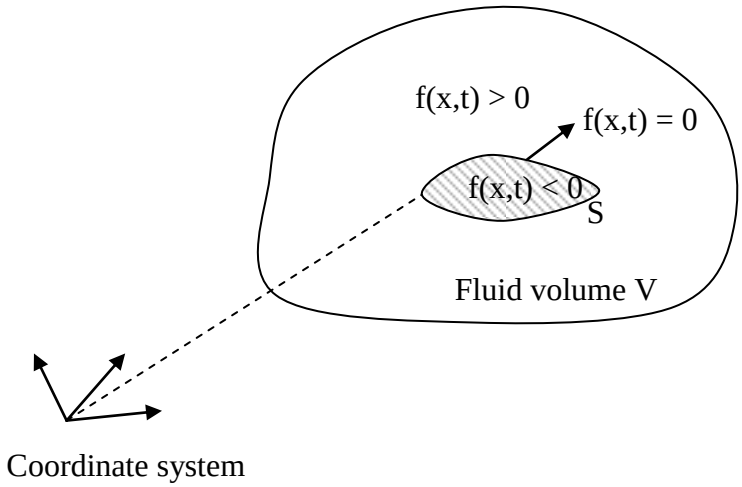

Figure 10 – FW-H Equation Model

The formulation of FW-H equation is similar to Lighthill's acoustic analogy. In other words, Navier-Stokes equations were rearranged into inhomogeneous wave equation by including monopole and dipole sources.

Continuity Equation:

$$\frac{\partial \rho}{\partial t} + \frac{\partial (\rho u_i)}{\partial x_i} = \rho_0 u_{s_i} \delta(f) \frac{\partial f}{\partial x_i} \tag{20}$$

Momentum Equation:

$$\frac{\partial (\rho u_i)}{\partial t} + \frac{\partial \left(\rho u_i u_j\right)}{\partial x_j} = -\frac{\partial p_{ij}}{\partial x_j} \tag{21}$$

In continuity equation, u_{s_i} is a point velocity field on the surface, f(x,t) = 0 is an equation of the kinematics of the surface and δ is the Dirac delta function.

By subtracting the space derivative of momentum equation from the time derivative of the continuity equation and with some arrangements, a new formula can be written in terms of the density fluctuation ρ' as follows

$$\frac{\partial^2 \rho'}{\partial t^2} - c_0^2 \frac{\partial^2 \rho'}{\partial x_i^2} = \frac{\partial}{\partial t}\left(\rho_0 u_i \delta(f) \frac{\partial f}{\partial x_i}\right) - \frac{\partial}{\partial x_i}\left(p_{ij} \delta(f) \frac{\partial f}{\partial x_j}\right) + \frac{\partial^2 T_{ij}}{\partial x_i \, \partial x_j} \qquad (22)$$

Equation (22) is the derivative form of Ffowcs Williams – Hawkings equation. The first term $\frac{\partial}{\partial t}\left(\rho_0 u_i \delta(f) \frac{\partial f}{\partial x_i}\right)$ on the right of Eqn. (22) is a monopole source which is the change of mass inside the control surface causing thickness noise. The second term $\frac{\partial}{\partial x_i}\left(p_{ij} \delta(f) \frac{\partial f}{\partial x_j}\right)$is a dipole source owing to the unsteady and steady forces exerted to the fluid by solid surfaces causing dipole noise or loading noise. The last term is quadrupole source because of the turbulent flow.

The $\delta(f)$ function in the monopole and dipole sources indicates that these two types of sources exist on the surface of the body. And quadrupole sources are available at outer of the body surface. There exist no kinds of sound sources inside the body.

The Ffowcs Williams – Hawkings equation, Eqn. (22), can be integrated analytically. For analytical solution, some assumptions are needed. These are the free space assumptions and the absence of obstacles between sound sources and the receivers. The complete solution of FW-H equation consists of surface integrals and volume integrals. The surface integrals are used to calculate monopole and dipole sources and partially quadrupole sources, while volume integrals are needed to determine quadrupole sources.

When the flow is low subsonic and the source region is enclosed by the source surface, the effects of the volume integrals in the Ffowcs Williams – Hawkings Equation becomes small. As a consequence, volume integrals can be dropped. In ANSYS FLUENT, volume integrals are skipped. To put it differently, ANSYS FLUENT uses the Porous FW-H equation consisting of no volume integrals instead of original FW-H equation.

3.2.3 The Porous Ffowcs Williams-Hawkings Equation

Since the contribution of the volume integrals in FW-H equation is negligible when the flow is subsonic and sound surface enclosures the source region, volume integrals can be dropped. Thus,

$$p'(\vec{x},t) = P_T{}'(\vec{x},t) + P_L{}'(\vec{x},t) \tag{23}$$

By using free space Green function, FW-H equation can be written for a moving control surface as follows:

$$4\pi p_T'(\vec{x},t) = \int_{f=0}\left[\frac{\rho_0\left(\dot{U}_n + U_{\dot{n}}\right)}{r(1-M_r)^2}\right]dS + \int_{f=0}\left[\frac{\rho_0 U_n\{r\dot{M}_r + c(M_r - M^2)\}}{r^2(1-M_r)^3}\right]dS \tag{24}$$

and

$$4\pi p_L'(\vec{x},t) = \frac{1}{c}\int_{f=0}\left[\frac{\dot{L}_r}{r(1-M_r)^2}\right]dS + \int_{f=0}\left[\frac{L_r - L_M}{r^2(1-M_r)^3}\right]dS + \frac{1}{c}\int_{f=0}\left[\frac{L_r\{r\dot{M}_r + c(M_r - M^2)\}}{r^2(1-M_r)^3}\right]dS \tag{25}$$

where

$$U_i = v_i + \frac{\rho}{\rho_0}(u_i - v_i) \tag{26}$$

$$L_i = P_{ij}\hat{n}_j + \rho u_i(u_n - v_n) \tag{27}$$

$$M_i = \frac{v_i}{c} \tag{28}$$

$u\ and\ v$ are the fluid velocity and the control surface velocity, respectively. M_i is the Mach number. The dot over a variable denotes source-time differentiation of that variable. And where

$$L_r = \vec{L}.\hat{\vec{r}} = L_i r_i \tag{29}$$

$$U_n = \vec{U}.\vec{n} = U_i n_i \tag{30}$$

When the integration surface coincides with an impenetrable wall, $P_T{}'(\vec{x}, t)$ and $P_L{}'(\vec{x}, t)$ are often referred to as thickness and loading terms, respectively. The square brackets denote that the kernels of the integrals are computed at the corresponding retarded times, τ, defined as follows, given the receiver time, t, and the distance to the receiver, r [24].

$$\tau = t - \frac{r}{c} \tag{31}$$

3.3 Boundary Layer Growth over a Flat Plate

When an incompressible fluid flow with uniform velocity, u, comes in contact with the trailing edge of the plate, fluid velocity becomes zero and the fluid particles are assumed to adhere to the plate surface in order to satisfy the no-slip condition. The fluid velocity rises rapidly from zero at the plate surface to the uniform velocity, called free stream velocity, within a short distance. As a result, extremely high velocity gradients are developed in the boundary layer causing high shear stresses. Thickness of the turbulent layer increases more rapidly than of laminar and transition layers. The outer of the turbulent boundary layer is the wake.

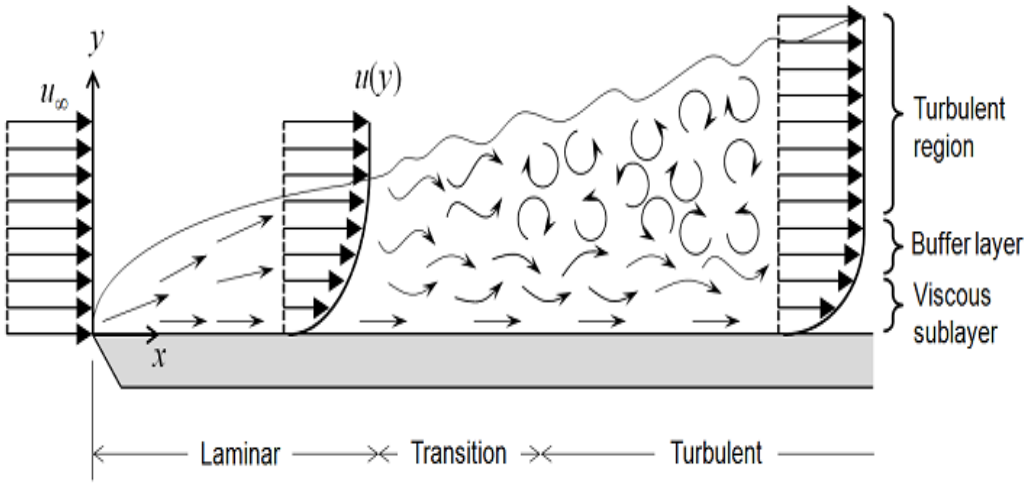

Figure 11 – Boundary layer development on a flat plate [25]

The outer edge of the boundary layer happens to be at which the fluid velocity in the x-direction within the boundary layer reaches 99 percent of the free stream. And the thickness of the boundary layer can be estimated as:

Laminar boundary layer thickness is given as

$$\delta_L = \frac{5x}{\sqrt{Re_x}} \tag{32}$$

Turbulent boundary layer thickness is given as

$$\delta_T = 0.05745\left(\frac{n^2 + 3n + 2}{n}\right)^{4/5} xRe_x^{-1/5} \tag{33}$$

where

$$n = \begin{cases} 7 & 5x10^5 < Re_x < 1x10^7 \\ 8 & 1x10^7 < Re_x < 1x10^8 \\ 9 & 1x10^8 < Re_x < 1x10^9 \end{cases} \quad (34)$$

The flow within the boundary layer is first laminar and then undergoes a transition from laminar to turbulent region. Transition region occurs between 300000 and 600000 Reynolds numbers [26]. Transition region is mostly affected by intensity, roughness of the surface, pressure gradient, curvature of the surface and so on.

The turbulent boundary layer is classified into inner and outer regions as shown in Figure 12. Inner region is subdivided into three layers. The flow is almost laminar in the viscous sublayer. Viscosity has a major role in momentum and mass transfer whereas turbulence plays a dominant role in the fully turbulent layer. In the buffer zone, the effects of viscosity and turbulence are equally significant.

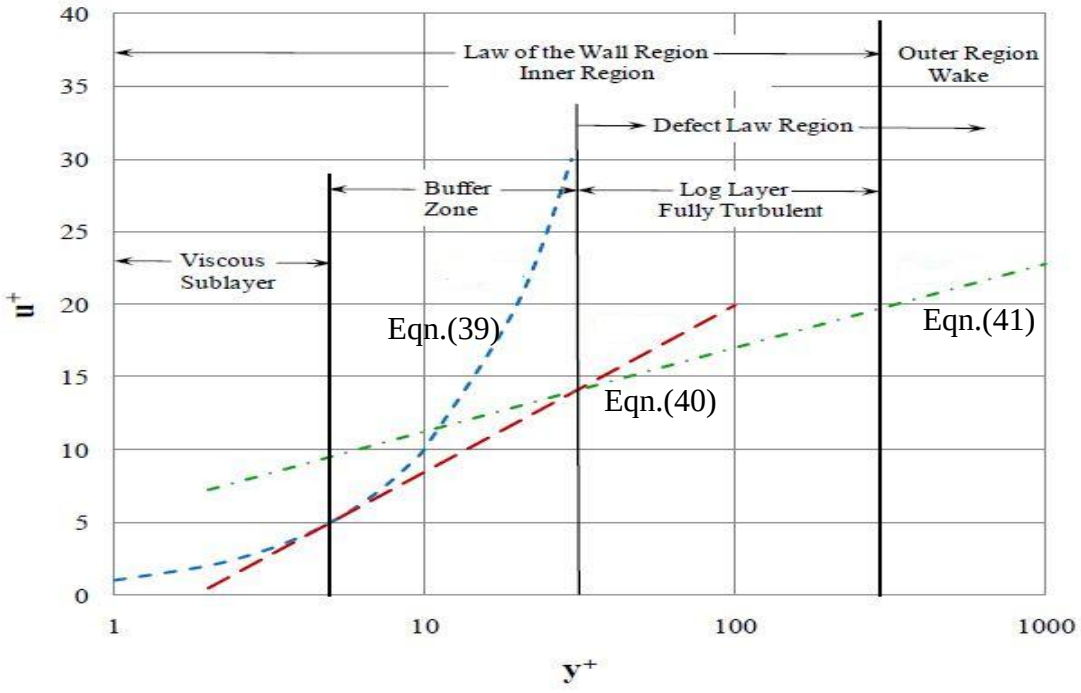

Figure 12 – Subdivision of turbulence region [27]

u^+ is a non-dimensional velocity and y^+ is a normal spatial surface coordinate. Their definitions are

$$u^+ = \frac{u}{U_\tau} \tag{35}$$

and

$$y^+ = y\frac{U_\tau}{v} \tag{36}$$

U_τ is the friction velocity given by

$$U_\tau = \sqrt{\frac{\tau_w}{\rho}} \tag{37}$$

Where τ_w is the shear stress at the wall and can be expressed for turbulent flow as

$$\tau_w = 0.0225\rho U_\infty^2 \left(\frac{v}{U_\infty \delta}\right)^{1/4} \tag{38}$$

Where ρ is the density, v is the kinematic viscosity, y is tha distance to the wall and τ_w is the shear stress at the wall. In the viscous sublayer, the relationship for near wall region is known as the law of the wall, while the relationship for the outer region is known as the defect law. The law of wall is empirically determined and the defect law is determined based on dimensional analysis and experimental observations. Law of the wall region and defect law region are combined together within the log layer.

In the viscous sublayer, the velocity profile is given as

$$u^+ = y^+ \tag{39}$$

In the buffer zone, velocity profile is

$$u^+ = 5lny^+ - 3.05 \quad (40)$$

In the turbulent layer, velocity profile is

$$u^+ = 2.5lny^+ + 5.5 \quad (41)$$

Eqn.(39), Eqn.(40) and Eqn.(41) are valid for incompressible flows over flat plates with zero pressure gradients.

3.4 Radiation by Simple Acoustic Source

The directivity of a sound source gives information about how the measured or predicted sound at a fixed distance varies with angular position. The directivity of the simple acoustic sources can be monopole, dipole and quadrupole.

3.4.1 Monopole

A monopole source radiates sound equally well in all directions. To put it differently, sound pressure does not change with respect to angular position at a fixed distance. The simplest example of a monopole source would be a small sphere whose radius alternately expands and contracts. The directivity pattern of a monopole source is shown in Figure 13.

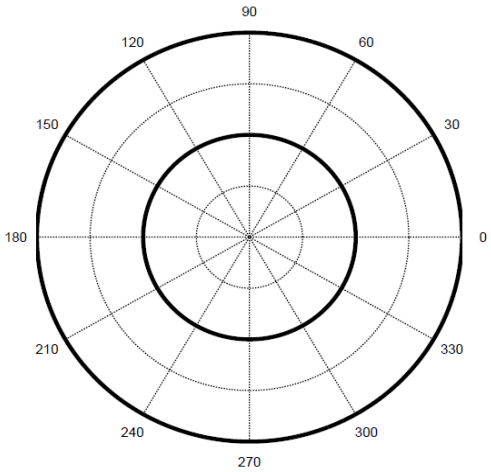

Figure 13 – Theoretical directivity patterns for sound pressure levels from a monopole

The radiated pressure p by a monopole at some distance r may be written as

$$p(r,\theta,t) = i\frac{Q\rho ck}{4\pi r}e^{i(2\pi ft-kr)} \tag{42}$$

and the pressure amplitude is then

$$|p(r,\theta,t)| = \frac{Q\rho ck}{4\pi r} \tag{43}$$

where ρ is the fluid density, c is the speed of sound, f is the frequency, r is the distance from the sound source, θ is the angular position, i is the imaginary number, t is the time, k is the wave number and Q is the complex source strength and represents the volume of the fluid displaced by the source.

3.4.2 Dipole

A dipole source consists of two monopoles of equal source strength but opposite phase and separated by a small distance with respect to wavelength of sound. In fact, the opposite phase means that while one source expands the other source

contracts. Consequently, a dipole source does not radiate sound in all directions equally.

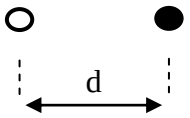

Figure 14 – Two monopoles of equal source strength but opposite phase

The radiated pressure p by a dipole at some distance r may be written as

$$p(r,\theta,t) = -i\frac{Q\rho ck^2 d}{4\pi r} cos\theta e^{i(2\pi ft - kr)} \tag{44}$$

And the pressure amplitude is then

$$|p(r,\theta,t)| = \frac{Q\rho ck^2 d}{4\pi r} cos\theta \tag{45}$$

The directivity pattern of a monopole source is shown in Figure 15.

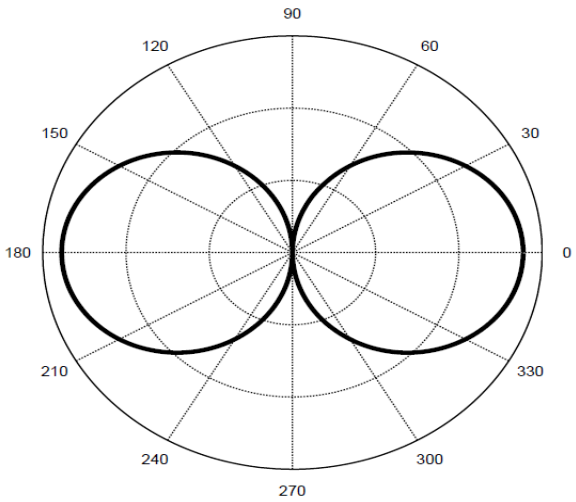

Figure 15 – Theoretical directivity patterns for sound pressure levels from a dipole

3.4.3 Quadrupole

A quadrupole source consists of two dipoles of equal source strength but opposite phase and separated by a small distance. Based on the arrangement of dipoles, quadrupoles can be classified into two categories, - lateral quadrupoles and longitudinal quadropoles**.**

3.4.3.1 Lateral Quadrupole

The dipole axes do not lie along the same line. The arrangement of dipole sources is shown in Figure 16.

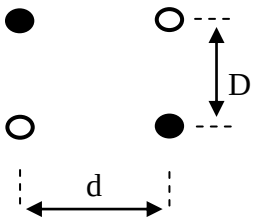

Figure 16 – Two dipoles of equal source strength but opposite sign in lateral arrangement

The amplitude of pressure p by a lateral quadrupole at some distance r may be written as

$$|p(r,\theta,t)| = \frac{Q\rho ck}{4\pi r} 4k^2 dDcos\theta sin\theta \qquad (46)$$

The directivity pattern of a lateral quadrupole source is shown in Figure 17.

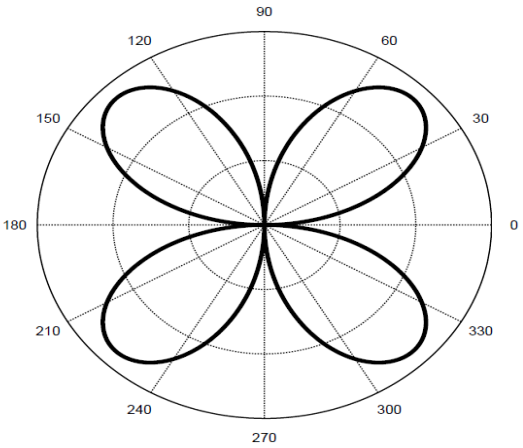

Figure 17 – Theoretical directivity pattern for sound pressure levels from a lateral quadrupole

3.4.3.2 Longitudinal Quadrupole

The dipole axes lie along the same line. The arrangement of dipole sources is shown in Figure 18.

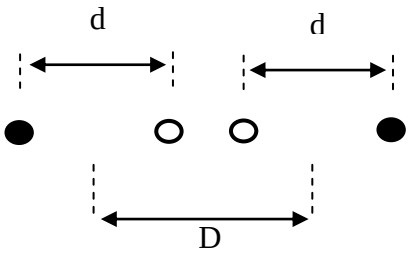

Figure 18 –Two dipoles of equal source strength but opposite sign in longitudinal arrangement

The amplitude of pressure p by a longitudinal quadrupole at some distance r may be written as

$$|p(r,\theta,t)| = \frac{Q\rho ck}{4\pi r} 4k^2 dD\cos^2\theta \qquad (47)$$

The directivity pattern of a longitudinal quadrupole source is shown in Figure 19.

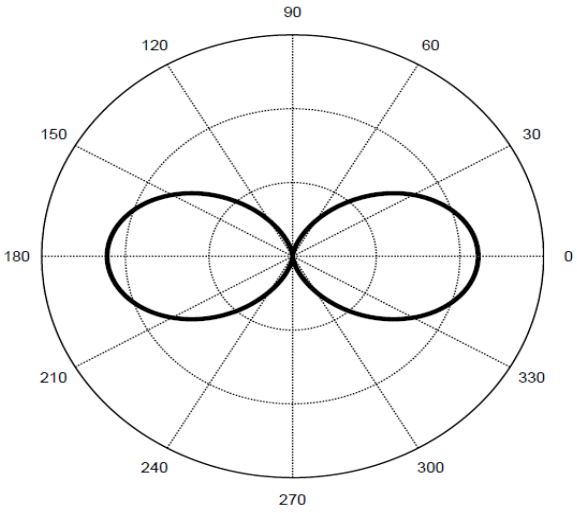

Figure 19 – Theoretical directivity pattern for sound pressure levels from a lateral quadrupole

CHAPTER 4

NUMERICAL ANALYSIS

4.1 Numerical Case

There are two configurations to be investigated in this study. These are:

Case A: only tube axial fan.

Case B: a blockage plate placed in front of the tube axial fan.

Case A is investigated theoretically and experimentally whereas Case B is studied only experimentally. Figure 20 shows Case A, 3D CAD of tube axial fan, and Figure 21 indicates Case B, tube axial fan with blockage plate.

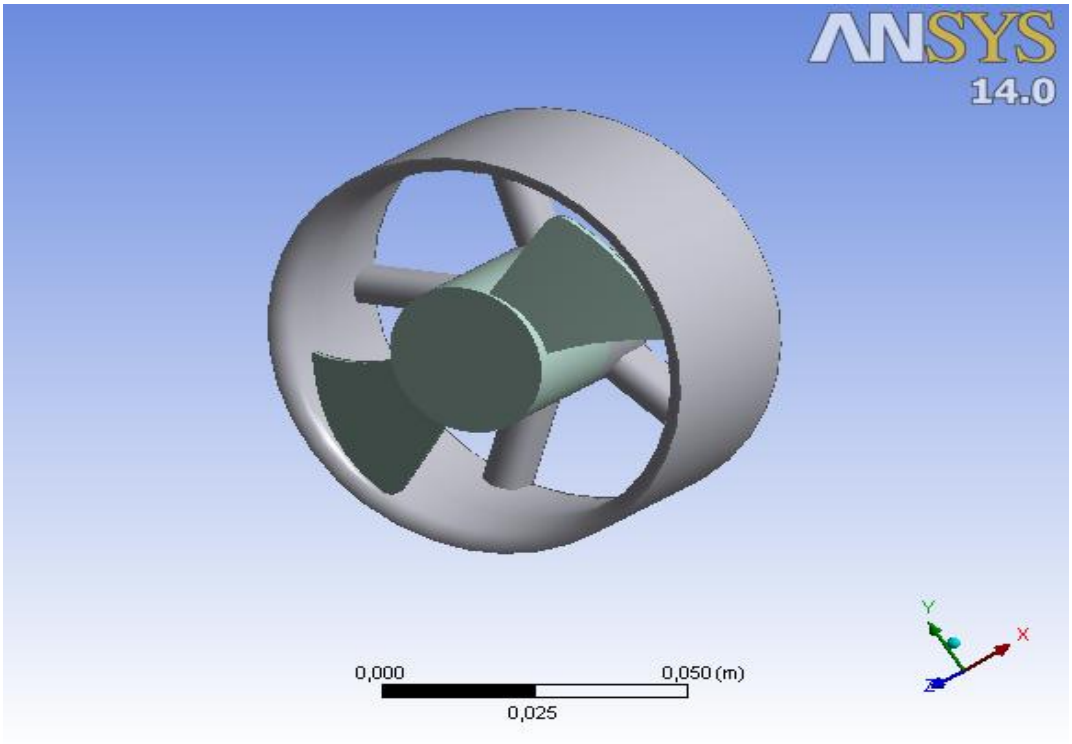

Figure 20 – Tube axial fan model – Case A

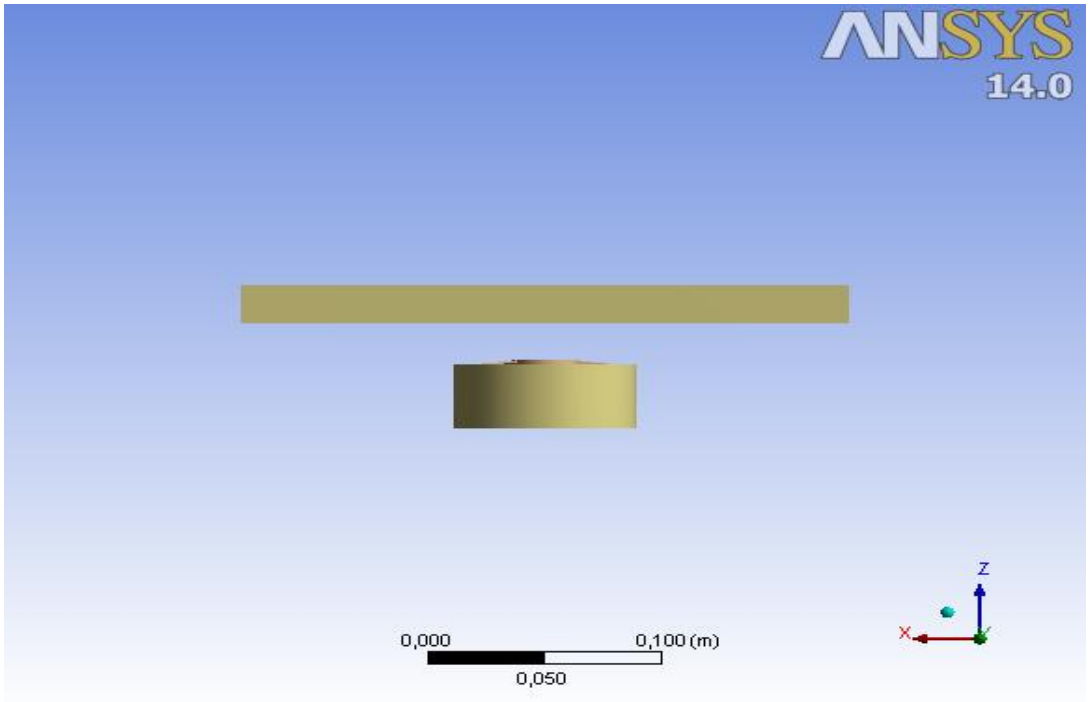

Figure 21 – A blockage plate in front of the tube axial fan- Case B

4.2 The Turbulence Model

Axial fan noise has both tonal and broadband characteristics. The tonal noise occurs at certain frequencies i.e. blade passing frequency and its harmonics owing to steady and unsteady flow loadings. On the other hand, broadband noise occurs at broad band frequency due to turbulent flow and aerodynamic forces.

In order to investigate axial fan noise numerically, there are some candidates of turbulence models which are Unsteady Reynolds Average Navier Stokes Equation (URANS), Large Eddy Simulation (LES) or Detached Eddy Simulation (DES).

URANS gives poor results in broadband noise; nevertheless, it gives reasonable results in tonal noise and on the ground to the fact that URANS does not need fine mesh as LES or DES, it does not need much computational time and effort, which makes it suitable most practical applications.

LES or DES gives better results in broadband noise than URANS inasmuch as LES or DES can capture larger turbulent eddies and filter the small turbulent eddies which URANS cannot. However, LES or DES needs very fine mesh and this increases computational time and effort which is too expensive for most practical applications. Performances of URANS and LES or DES are compared in Table 1.

Table 1 – Comparison between URANS and LES or DES

	URANS	LES or DES
Broadband noise	Poor	Good
Tonal noise	Good	Good
Mesh	Medium	Fine
Computational power	Low	High

In this study, the first revolution of transient solution of the fan is done to achieve steady state and a further 5 revolutions are done to obtain acoustical data. These 6

revolutions require different computational power and time for URANS and LES or DES while URANS needs the least computational power and time.

The tube axial fan used in this study has two blades and its rotational speed is 21000 rpm. Since rotation speed is very high, the dominant noise is expected to be the tonal noise. Blade Passing Frequency (BPF) and its harmonics can be calculated as follow:

1^{st} of BPF = $\frac{2x21000\ \text{rpm}}{60\ \text{s}} = 700\ \text{Hz}$

2^{nd} of BPF = $2x700 = 1400\ \text{Hz}$

3^{rd} of BPF = $3x700 = 2100\ \text{Hz}$

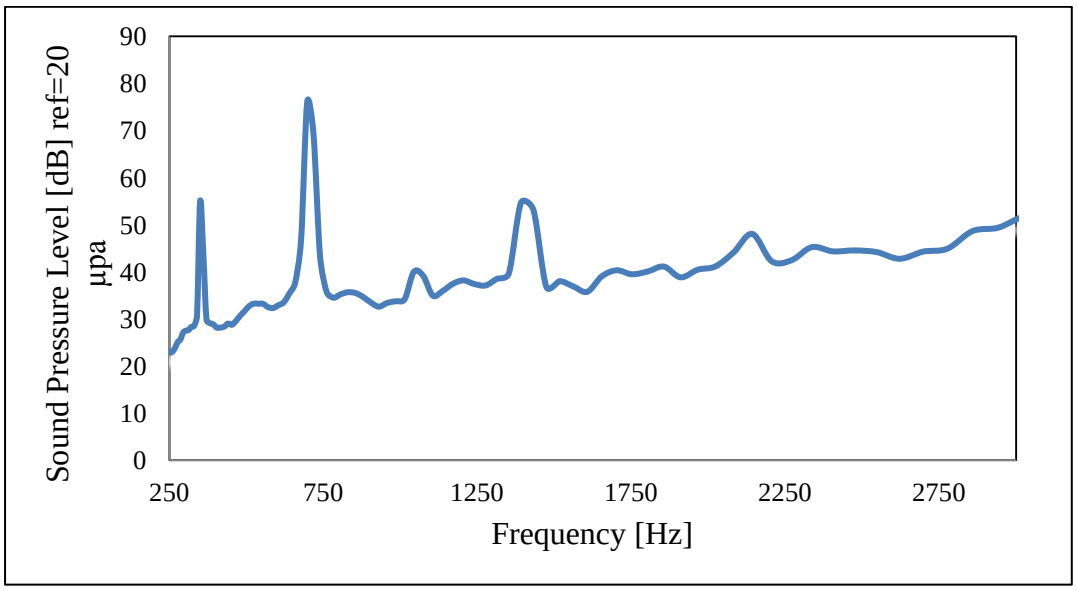

Figure 22 – Experimentally measured SPL of the tube axial fan noise (rotational speed = 21000 rpm and measured at 1 m away from the inlet fan axis)

In Figure 22, the second peak is the first harmonic of BPF and the third peak is the second harmonic of BPF and the fourth peak corresponds to the third BPF. The first peak corresponds to the frequency of rotational speed of the tube axial fan. According to the Figure 22, since sound pressure levels at broadband are lower, at

21000 rpm of fan rotational speed, the dominant noise is the tonal noise and this supports the expectation.

To conclude, due to limited computational power and time and interested characteristic of noise - tonal noise-, URANS is selected for turbulence model in this study.

4.3 Modeling of Fluid Volumes

In this study, ANSYS 14.0 Fluent program is used to investigate tube axial fan noise numerically. Geometric model is generated by Pro/E Creo Parametric 2.0 and then imported to ANSYS Design Modeler. The geometric model has three volumes; namely, rotating part, acoustic source domain part and stationary part given in Figure 23. The geometric specifications of the tube axial fan are given in Table 2.

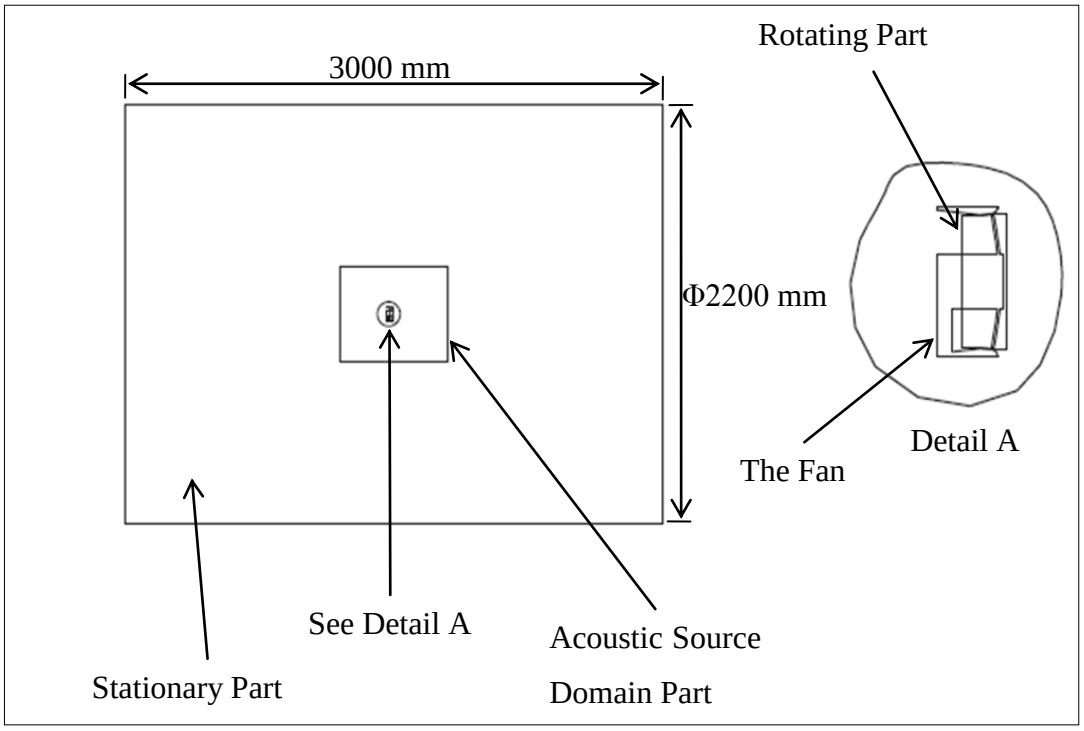

Figure 23 – Geometric model of the fluid volumes

Table 2 – The geometric specifications of the tube axial fan

Blade geometry	
Blade number	2
Tip diameter (mm)	69
Hub diameter (mm)	29
Case inner diameter (mm)	71
Chord length (mm)	3

4.4 Meshing of Fluid Volumes

The unstructured tetrahedral mesh for fluid volumes is generated in ANSYS Meshing Modeler. For URANS turbulence model, maximum mesh size should not exceed one-sixth of the acoustical wavelength whose frequency is the highest frequency of interest [29], [31]. In this study, the largest interested frequency is 3000 Hz, which makes the maximum element size 19 mm. In this study, the maximum element size is taken as 14 mm corresponding approximately one-eighth of the acoustical wavelength whose frequency is 3000 Hz and minimum element size is taken as 0.5 mm.

The blades of the tube axial fan are meshed with tetrahedral elements as shown in Figure 24. Boundary layer meshes are applied to the blades of the tube axial fan so as to capture turbulent flow near the surfaces of the fan blades as shown in Figure 25. Edge size of the blades of the tube axial fan is adjusted to a value of 0.1 mm. First layer height of the boundary layer mesh is 0.003 mm with a 1.2 growth rate and the number of boundary layers is 27 corresponding boundary layer thickness is about 2 mm. As a result, number of mesh is approximately 6.7 million and average skewness is 0.21.

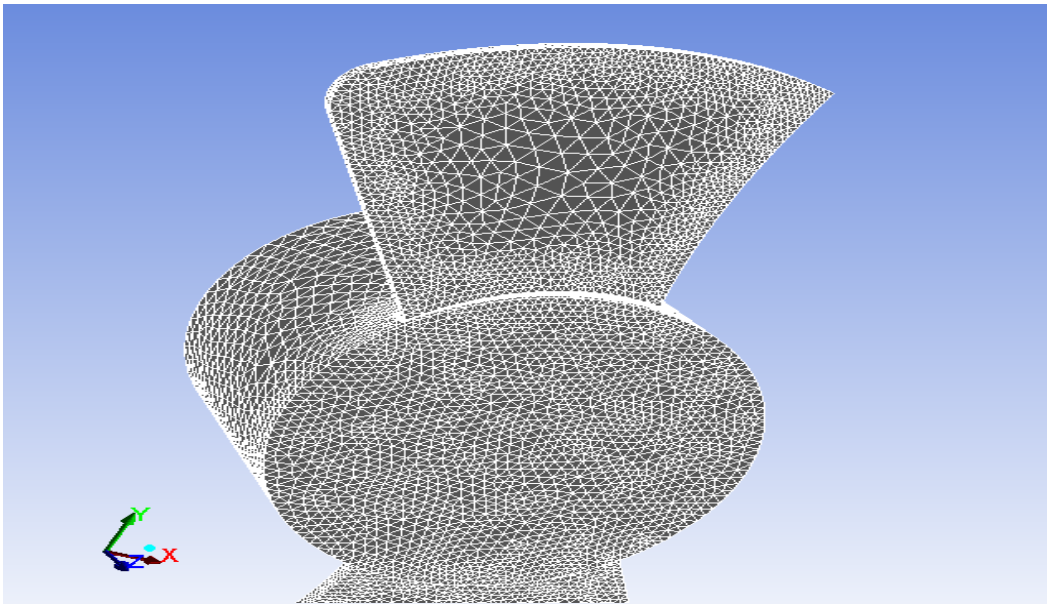

Figure 24 – Unstructured tetrahedral mesh of the blade surface of the tube axial fan

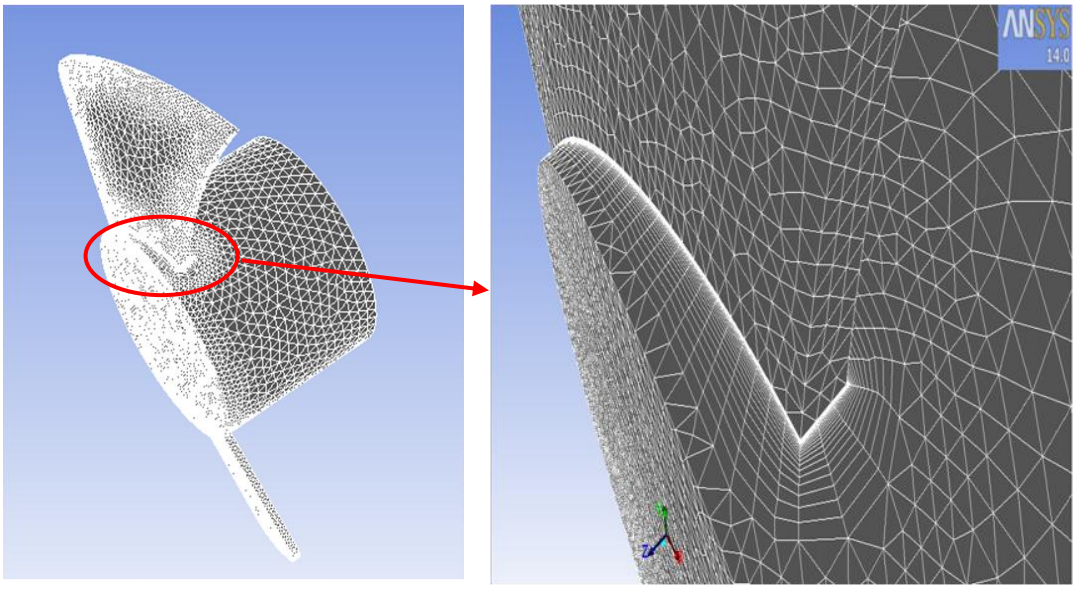

Figure 25 – Boundary layer mesh of the blade of the tube axial fan

S. Marburg [31] investigated sound generated inside a sedan cabin compartment with three different mesh configurations whose maximum element sizes are different and smaller than one-sixth of wavelength length whose frequency is

maximum frequency of interest. Among these three mesh configurations, coarsest mesh obtains sound pressure levels with an error lower than half a decibel. Hence, only one single mesh configuration is applied in this study. Furthermore, first boundary layer height and boundary layer thickness are good enough since it is proved that after the numerical solution, wall y^+ values of the blades of the tube axial fan are lower than 1.

4.5 Transient Flow Solution Procedure

Fluent 14.0 software is used for computational fluid dynamics (CFD) and for computational aero acoustics (CAA). The flow is assumed to be incompressible since Mach number (M=0.22) is less than 0.3.

The fan rotational speed $\Omega = 21000 \text{ rpm} = 350 \text{ Hz}$

The radius of the fan $r = 34.5 \text{ mm}$

Speed of the tip of the fan $u = \Omega x r = 75.87 \frac{m}{s}$

Mach number $M = \frac{u}{c_0} = \frac{75.87}{346} = 0.22$

Realizable k-ε with Enhanced Wall Treatment function is preferred as a viscous model. According to FLUENT documentation, realizable k-ε turbulence model is superior to standard k-ε and RNG k-ε turbulence models. Moreover, D. Saatchi et al. [30] investigated the trailing edge noise of NACA0012 airfoil by applying realizable k-ε turbulence model with FW-H acoustics model and their numerical results are in fair agreement with the experimental data.

The SIMPLE algorithm is applied in order to couple velocity and pressure because SIMPLE algorithm needs less computational effort. Turbulent kinetic energy and turbulent dissipation rate are defined as second order upwind.

Boundary conditions are applied such that inlet velocity is taken as 0.001 m/s and the total pressure at outlet is atmospheric pressure, which makes gauge pressure

zero. Symmetry condition is applied on the outer cylinder shell. Rotating part volume including the blades of the fan is defined as rotating with 21000 rpm. The wall consisting of the blades of the fan is defined as stationary with respect to rotating part. The other walls and volumes are stationary and have no slip conditions.

While defining velocity inlet and pressure outlet boundary conditions in FLUENT, hydraulic diameter and turbulence intensity values are needed, as well and they are given in Table 3 and Table 4 for both inlet and outlet boundary conditions. Hydraulic diameter for velocity inlet and pressure outlet is equal to the diameter of the inlet surface and of outlet surface, respectively. Hydraulic diameter at inlet and outlet are the same being equal to 2.2 m. Then, the turbulent intensity is taken as 5%.

Table 3 – Inlet Boundary Condition

Condition	Value
Velocity	0.001 m/s
Hydraulic Diameter	2.2 m
Turbulent Intensity	5%

Table 4 – Outlet Boundary Condition

Condition	Value
Gauge Pressure	0 Pa
Backflow Hydraulic Diameter	2.2 m
Backflow Turbulent Intensity	5%

Acoustic source is defined as the enclosed interior surface of the acoustic source domain part. This enclosed interior surface includes body surfaces and turbulent flows inside. Therefore, all body surfaces and turbulent flows inside the permeable surface are taken as sound sources. In other words, all monopole, dipole and quadrupule sources inside this enclosure surface are taken into account. However,

the complete solution of FW-H equation needs surface integrals and volume integrals. Surface integrals are utilized to predict monopole, dipole and partially quadrupole sound source, whereas volume integrals are applied to determine quadrupole sound source. Since the effect of quadrupole noise is small, volume integrals are dropped in FLUENT. Time step is set as 1.25×10^{-5} s and every time step corresponds to 1.58° increment of a full rotation of the tube axial fan. Acoustical data are saved at every time step during the transient analysis for 5 revolutions of the fan at which one time period of the speed of the tube axial fan is 2.86 ms. Consequently, total time length of acoustical data becomes 14.3 ms as shown in Table 5. After the transient analysis finishes, receivers are defined at the same locations as the locations of the microphone in the experiment of sound measurement. Finally, sound pressure levels are calculated at the defined receivers.

Table 5 – Time Integration Scheme

Condition	Value
Time Step	1.25×10^{-5} s
Time Period of One Rotation	2.86 ms
Time Length of Acoustical Data	14.3 ms

The CFD and CAA simulations can be divided into three parts. In the first part, a steady-state RANS is performed to give an initial guess for unsteady RANS in order to decrease the convergence time of unsteady RANS. In the steady-state RANS simulation, standard k-ε turbulence model is used and rotating part is selected as rotating reference frame. In the second part, an unsteady RANS with an initial guess from the first part for 1 revolution is performed to reach a stationary flow field. The realizable k-ε viscous model is used and sliding mesh is applied to the rotating part. Finally, the realizable k-ε viscous model and the FW-H acoustics model are employed to compute the unsteady flow and sound generated, respectively. Here, acoustical data is recorded for 5 revolutions.

The total computational time with 2 processors, 16 cores and 64 GB installed memory (RAM) for 6.7 million number of mesh, realizable k-ε turbulence model

coupled with FW-H acoustics model and sliding mesh technique is approximately 18 days.

Figure 26 indicates steps of procedures of the numerical analysis of the noise of the tube axial fan in FLUENT 14.0.

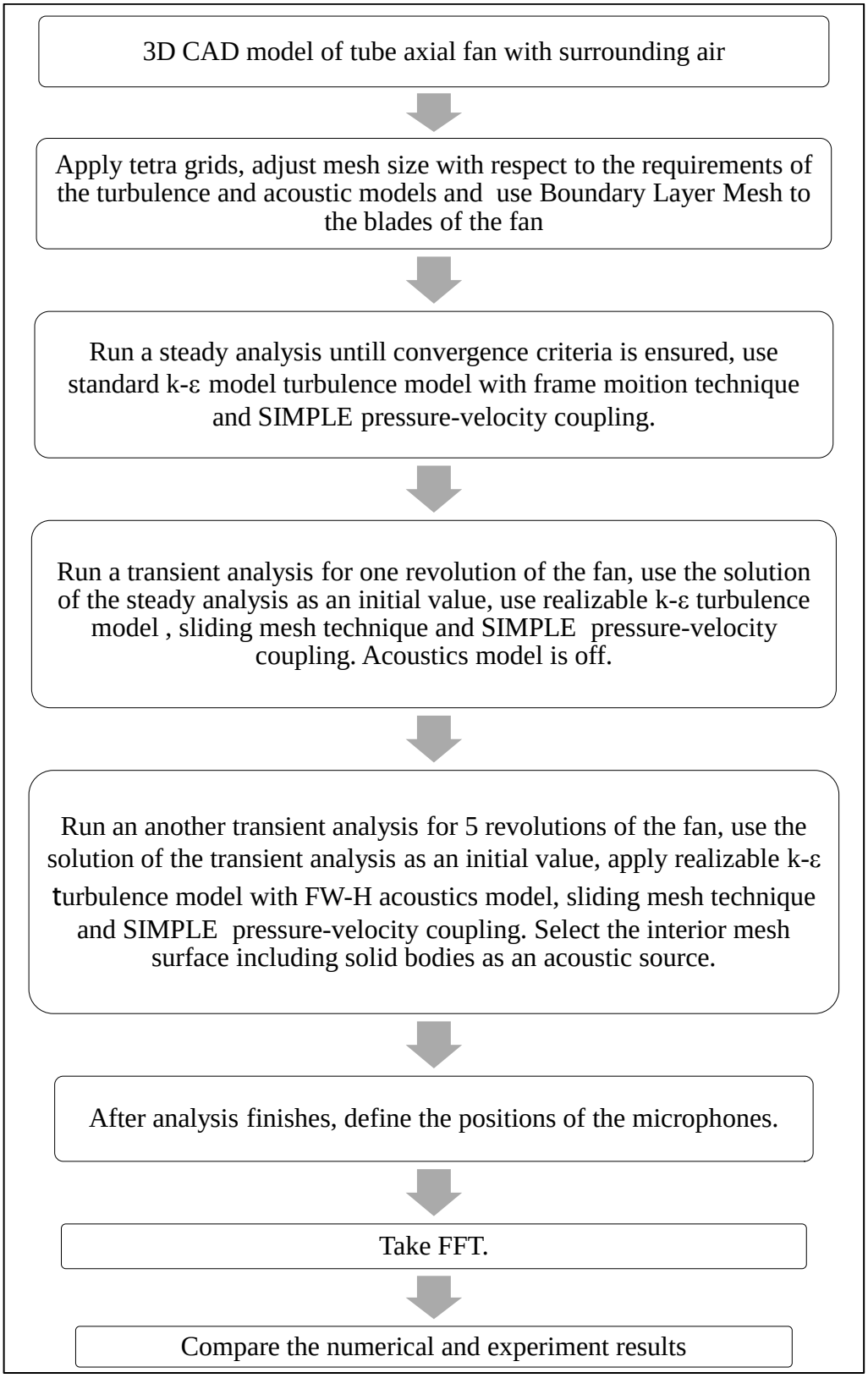

Figure 26 – The procedures of the numerical analysis of the noise of the tube axial fan in FLUENT 14.

CHAPTER 5

EXPERIMENTAL METHODOLOGY

5.1 Test Facilities

The acoustic measurements are performed in the Semi-Anechoic Room of ASELSAN A.Ş. in Akyurt, Ankara The dimension of the semi-anechoic room is 9 m in height, 11 m in width and 20 m in length. The cut- off frequency of the semi-anechoic room is

$$f_{cut-off} = \frac{344 \frac{m}{s}}{0.3\ m\ x\ 4} = 287\ Hz \tag{48}$$

5.2 Sound Pressure Level (SPL) Measurements

Acoustic measurements are carried out for Case A and Case B. In Case A, the sound pressure levels (SPL) of the tube axial fan alone and in Case B, SPL of the tube axial fan adjacent a blockage plate are measured at different microphone positions in the far field. The fan is positioned in one of the corners of the semi-anechoic room, 1.5 meters above from the reflecting surface. The microphone is positioned at a 2-meter diameter circle whose center coincides with the fan, 1.5 meters above from the reflecting surface since it is indicated in ISO-3744 that the sound source should be at least 1.5 m away from the

reflecting surface. The microphone is positioned with a 30-degree increment, that is, SPL is measured at 12 different positions. The microphone positions are shown in Figure 27.

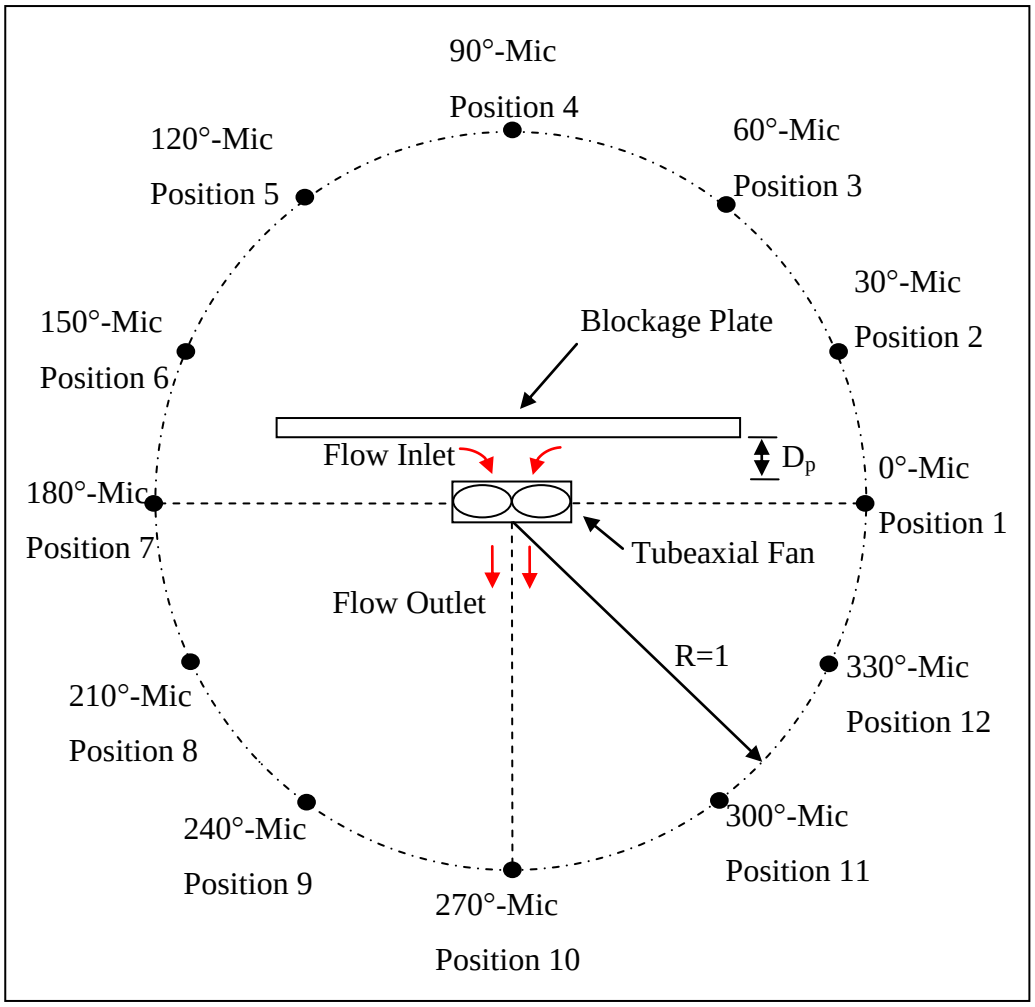

Figure 27 – Model of experimental set-up (not to scale)

Dp is the distance between the tube axial fan and the blockage plate. SPL of the Case B is measured for Dp = 18.4 mm. The rotation axis of the tube axial fan is in coincidence with the center of the blockage plate as shown in Figure 28.

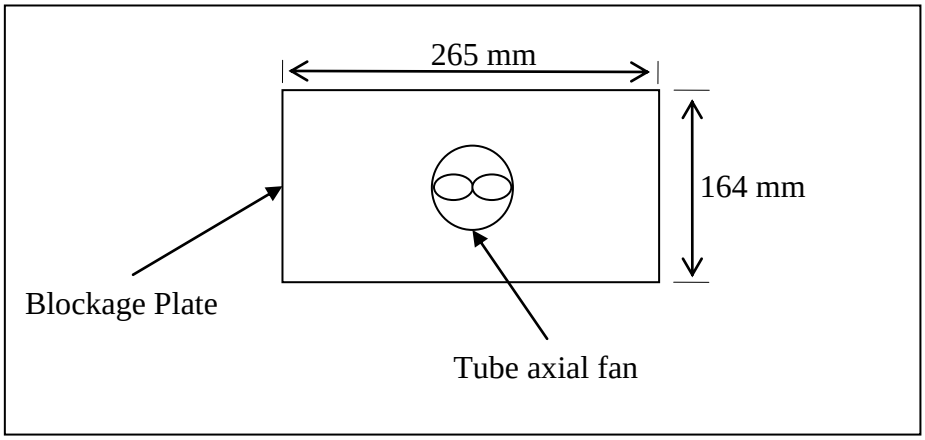

Figure 28 – Configuration of tube axial fan with blockage plate

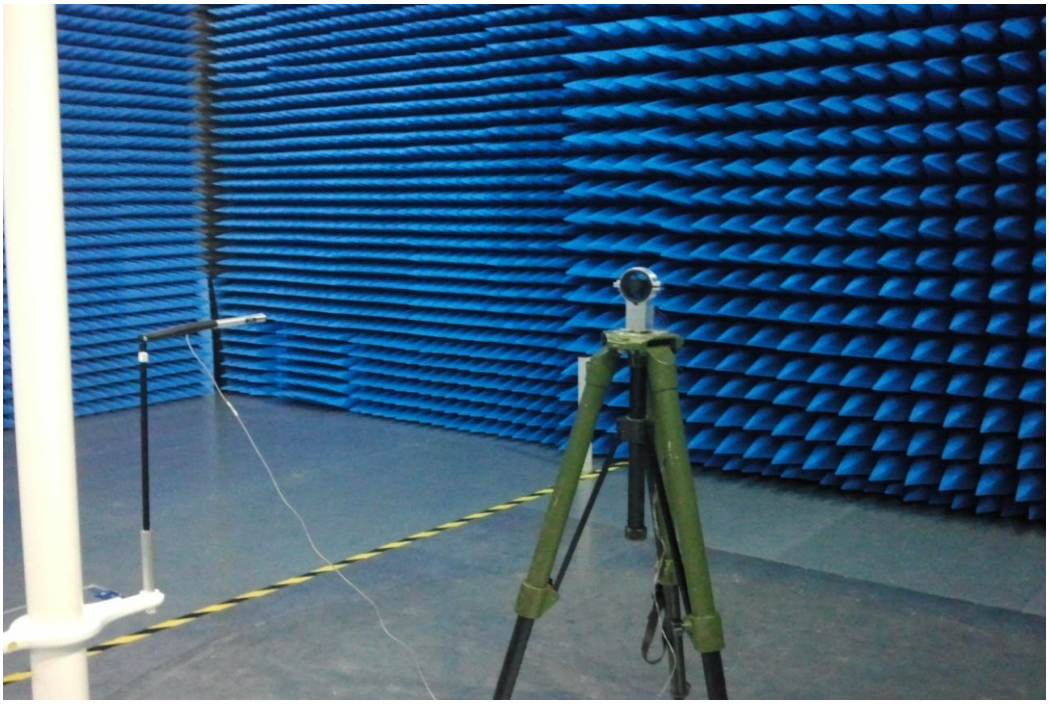

Figure 29 – SPL measurement set-up of the tube axial fan in semi-anechoic room.

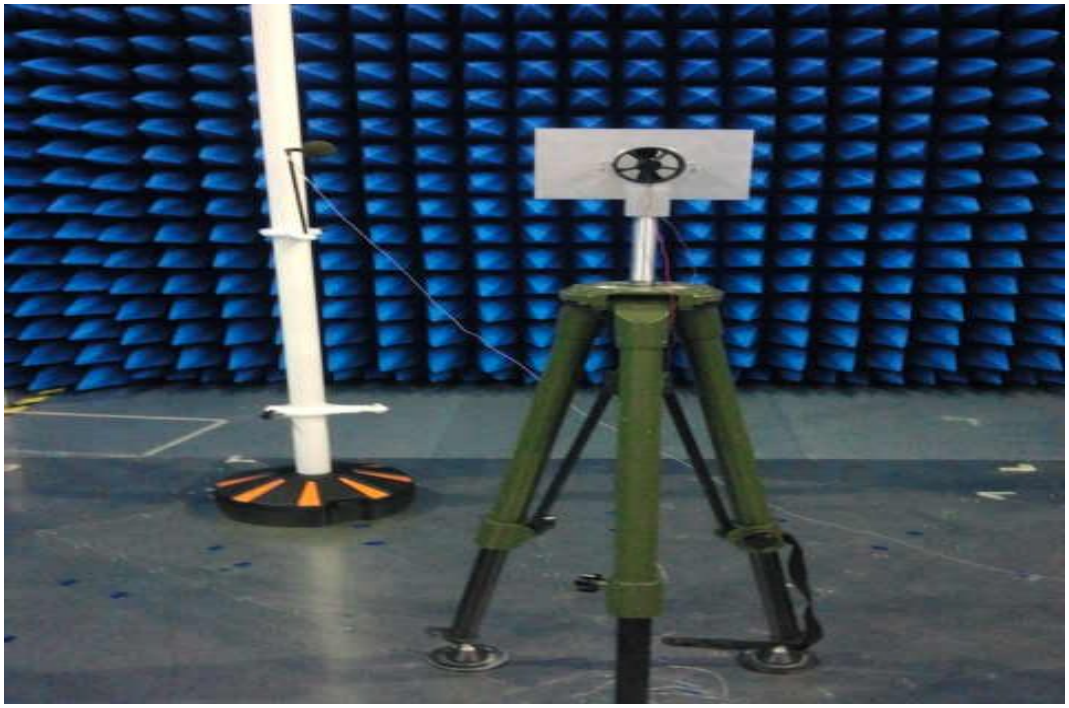

Figure 30 – SPL measurement set-up of the tube axial fan adjacent a blockage plate in semi-anechoic room.

According to ISO-3744, SPL of the background noise should be preferably 15 dB less than SPL of the measured sound at corresponding frequency range of interest. As it can be seen from Figure 31, broadband noise of background is at least 15 dB less than broadband noise of the fan in the frequency range of interest, which is from 250 Hz to 3000 Hz.

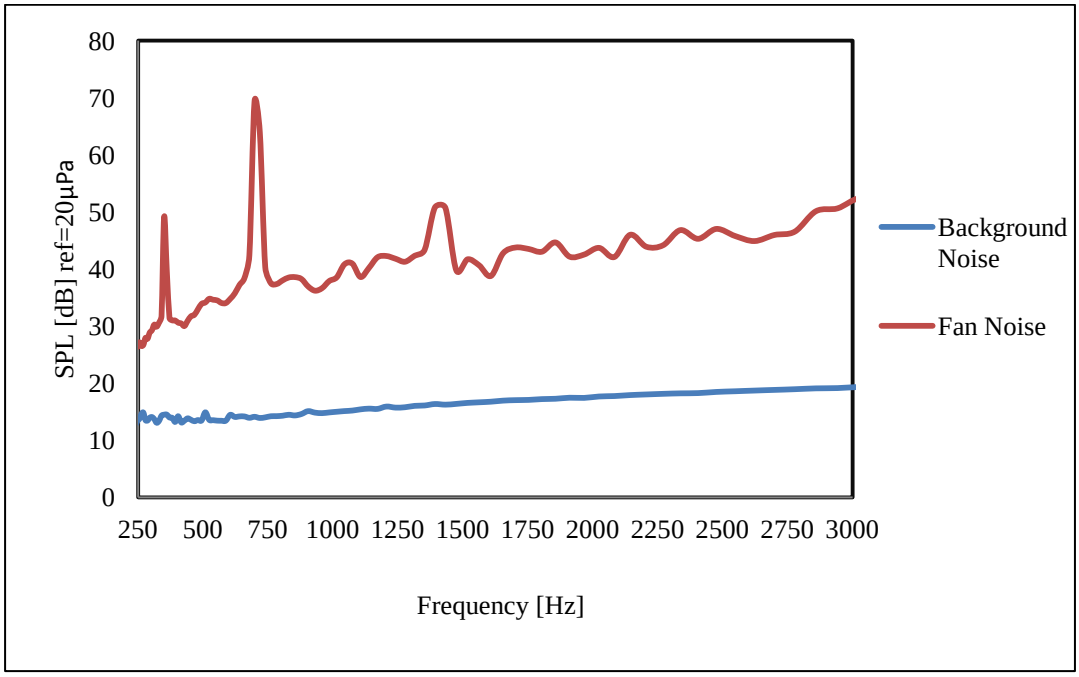

Figure 31 – Measured SPLs of noise of background and of Tube axial fan at 90° microphone position in the range of frequency of interest

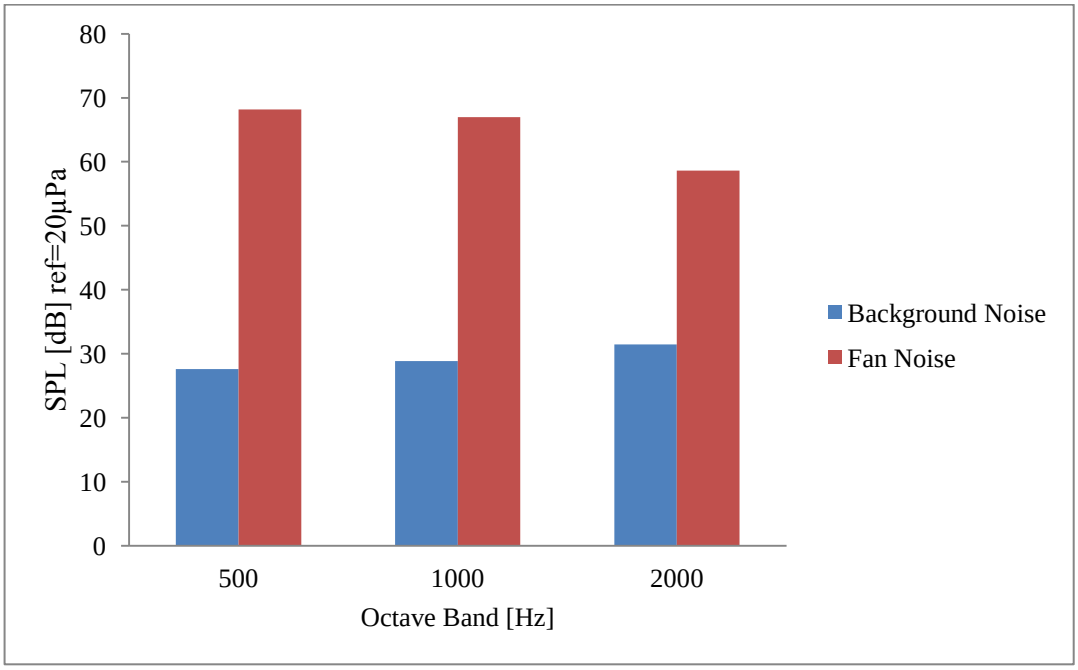

Figure 32 – Octave band of SPLs of noise of background and of Tube axial fan at 90° microphone position.

5.2.1 Instrumentation

The acoustic measurements are performed with B&K PULSE 3560 data acquisition system, B&K 4938-A-011 ¼ inch Microphone and Panasonic CF-31 Toughbook computer which does not possess a cooling fan. The software is 17.0 PULSE Labshop by B&K.

A wind shield is put on the microphone so as to eliminate the effects of interaction of air flow with microphone inasmuch as interaction of air flow with microphone generates additional noise.

5.2.2 Analyzer Setting Procedure

For analyzer settings, the steps below are followed:

1. Select 1/24 octave band
2. Define the data acquisition channels
3. Adjust the measurement duration as 120 s.
4. Select reference sound pressure as $20x10^{-6}$ Pa
5. Input maximum frequency of interest as 16 kHz.
6. Select Hanning window
7. Start recording

5.2.3 Measurement Methodology

Before measurement, some preparations should be done as follows:

1. Prepare analyzer setting as describe above in the Analyzer setting section
2. Place the fan and the microphone on the platform
3. Adjust the speed of the fan around 21000 rpm

4. Run the fan at a speed of 21000 rpm for 30 minutes to reach the steady-state conditions
5. Start recording
6. Record the humidity and temperature during the measurement.

CHAPTER 6

RESULTS OF NUMERICAL AND EXPERIMENTAL STUDIES

6.1 Convergence of Flow Solution

The default convergence criterion in FLUENT is that the residuals must decrease to 10^{-3}. In this study, the default convergence criterion defined in FLUENT is applied. The default convergence criterion value in FLUENT is defined as 10^{-3}.

However, even though the convergence criterion defined in FLUENT is satisfied, it may sometimes be insufficient. Thus, the change of static pressure of a point inside the casing and in front of pressure side of one of the blades during the recording of the acoustical data are monitored and given in Figure 33 and Figure 34, respectively.

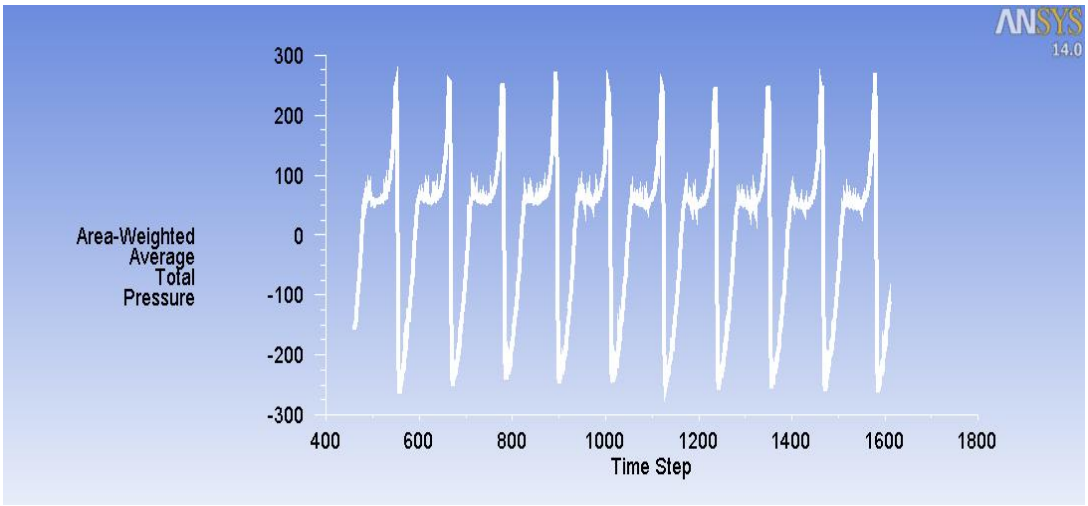

Figure 33 - Area weighted static pressure of a point inside the casing of the tube axial fan

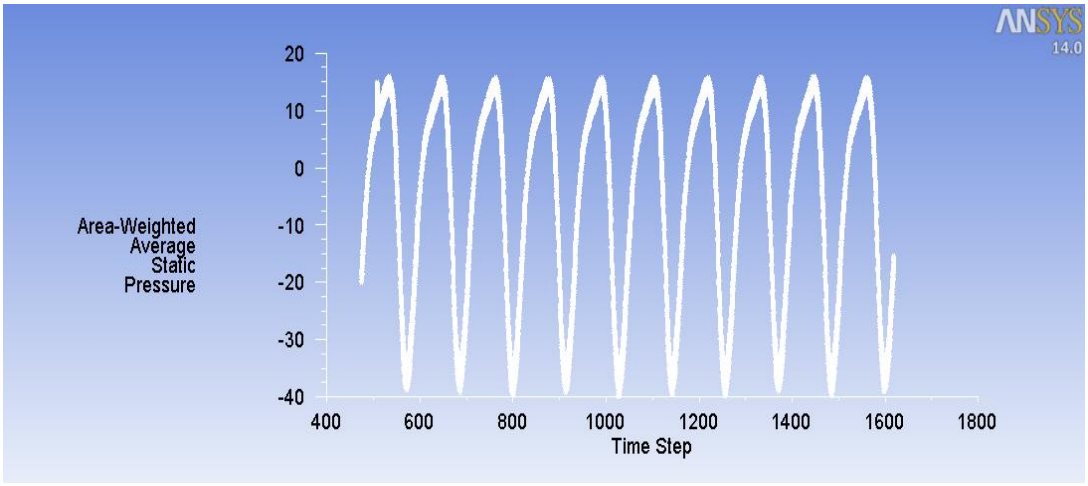

Figure 34 - Area weighted static pressure of a point in front of the pressure side of one of the blades of tube axial fan

Since the static pressure has the same trend for each revolution of the fan as indicated in Figure 33 and Figure 34, the solution is assumed to converge.

6.1.1 Wall Y^+ Values of the Surfaces of the Fan Blades

Wall y+ values of the surfaces which have significant effect on the flow should be lower than 1 while using enhanced wall treatment function. This criterion is satisfied as shown in Figure 35. The blades of the tube axial fan have wall y+ values lower than 1.

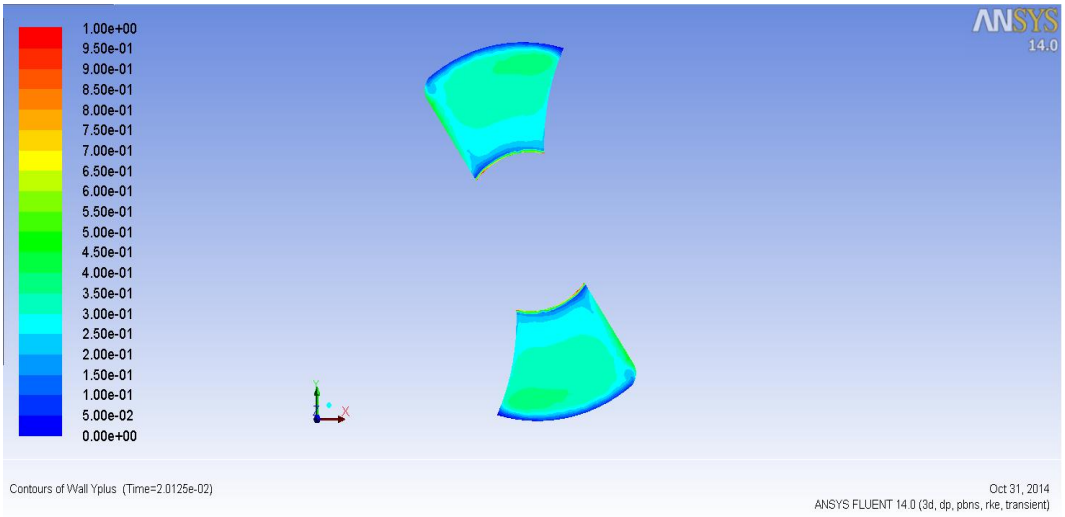

Figure 35 – Wall y+ values of the blades of the tube axial fan

6.2 The Pressure Distribution of Tube Axial Fan

The pressure contours of the tube axial fan and leading edge of the fan blade are indicated in Figure 36 and Figure 37, respectively.

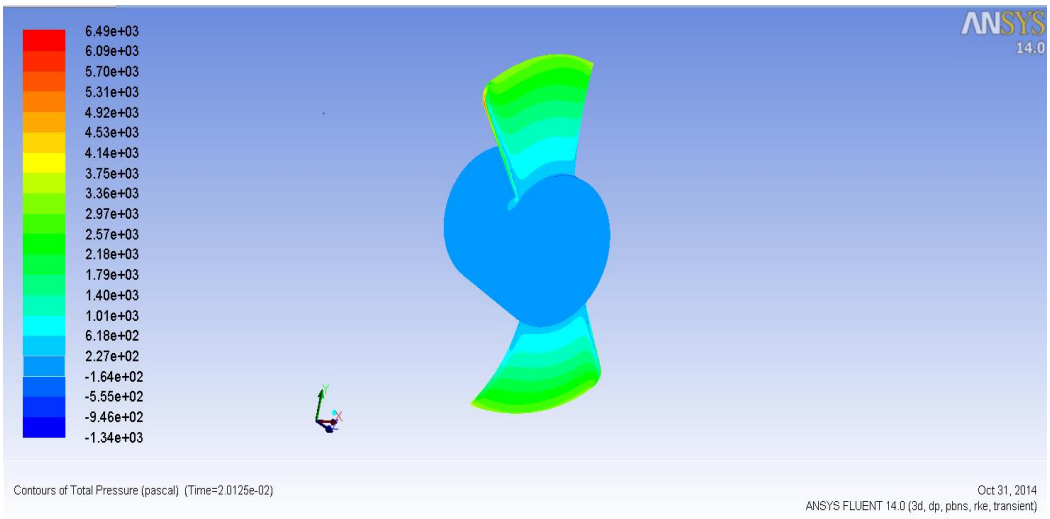

Figure 36 – Pressure distribution of the tube axial fan

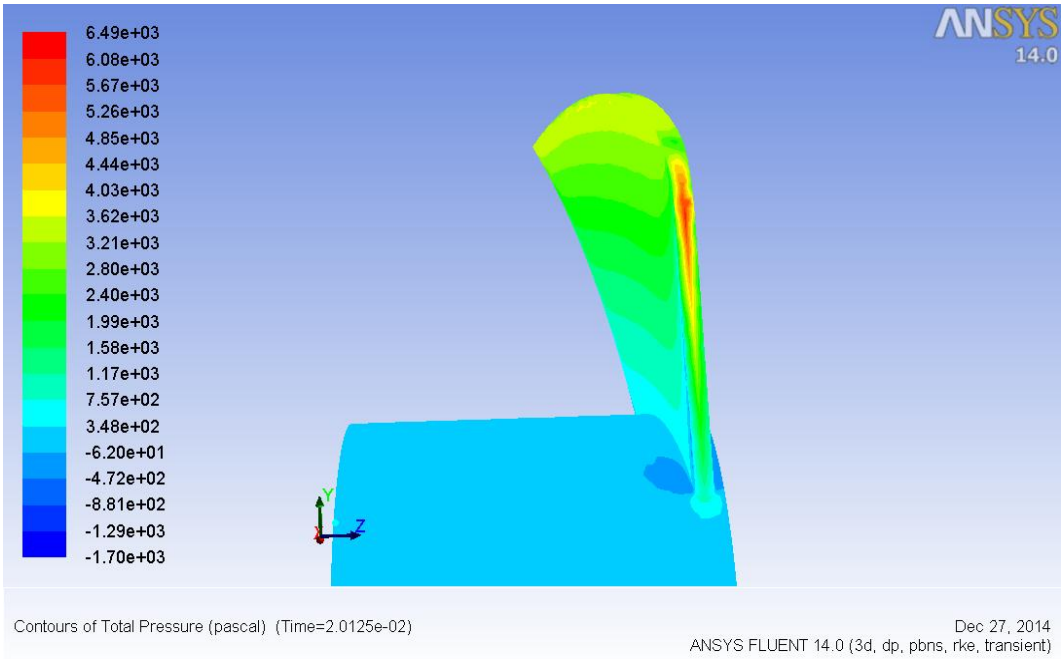

Figure 37 – Pressure distribution of the leading edge of the fan blade

The maximum pressure on the blade of the tube axial fan occurs at the leading edge near the tip of the blade on which the fan noise mostly depends.

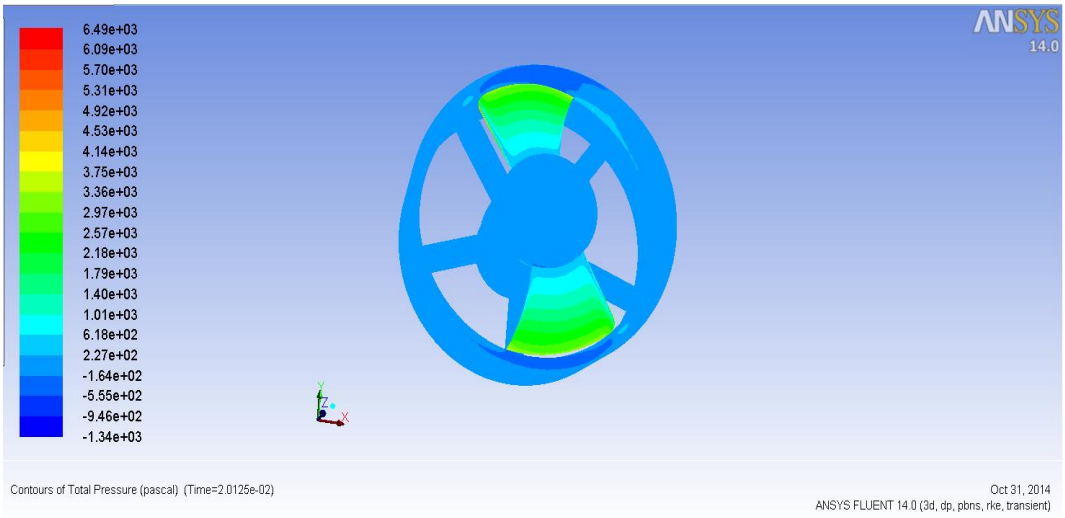

Figure 38 – Pressure distribution of the tube axial fan with casing

The pressure contour of tube axial fan with casing is indicated in Figure 38. The pressure distribution on the casing indicates that the flow inside the casing has a helical shape. In other words, the air leaving the tip of the blades moves in a spiral curve inside the casing.

6.3 The Comparison of Numerical and Experimental Noise of Tube Axial Fan

6.3.1 The Comparison of Numerical and Experimental Sound Spectrum of Tube Axial Fan at the First Three BPFs

The predicted and measured sound pressure levels of the tube axial fan at the first BPF are shown in Figure 39 and the predicted and measured relative directivity pattern of the tube axial fan at the first BPF are shown in Figure 40.

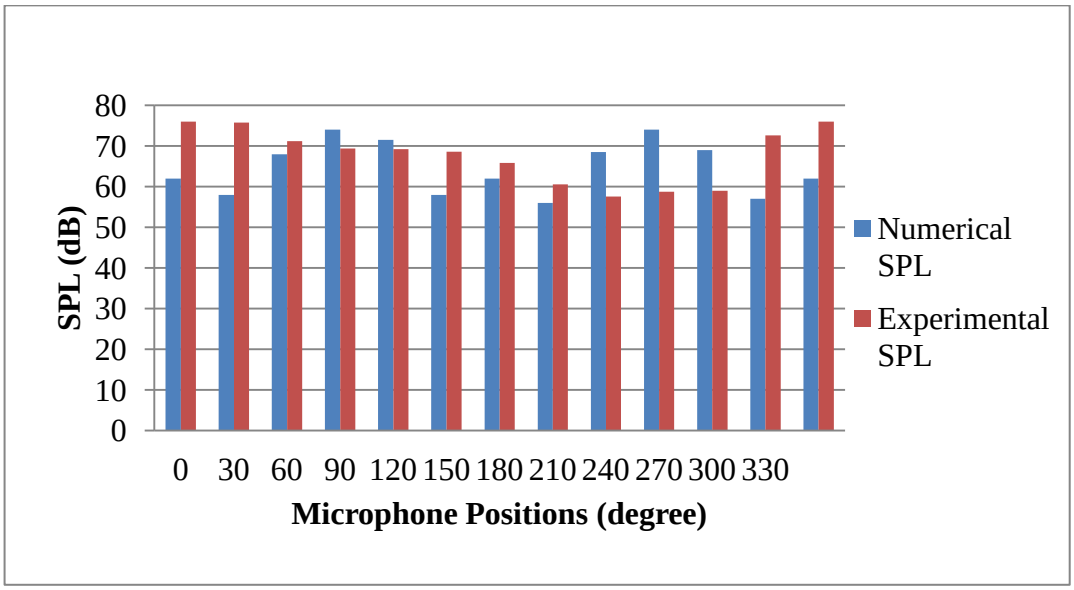

Figure 39 – Predicted and measured sound pressure levels of the tube axial fan at the first BPF

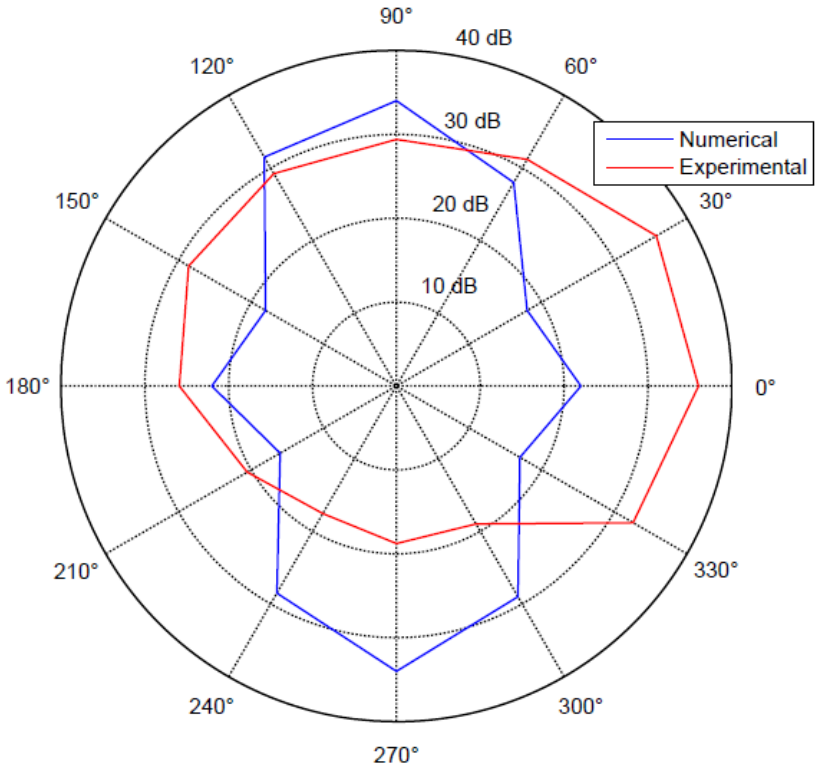

Figure 40 – Relative directivity of predicted and measured SPL of the tube axial fan at the first BPF

According to Figure 40, the measured directivity of the tube axial fan at the first BPF is anisotropic. The maximum SPL of the first BPF of the tube axial fan was measured at 0° microphone position. As a result, directivity of the tube axial fan at the first BPF cannot be simply defined in terms of monopole, dipole or quadrupole radiation patterns. The reason for this anisotropy may be due to the asymmetries in the tube axial fan itself since effects of asymmetries becomes significant at very high rotational speed of the tube axial fan and the other reason might be attributed to that the tube axial fan motor noise affects the directivity of the tube axial fan at low frequencies. On the other hand, FW-H equation seems to give the directivity pattern of the tube axial fan noise as dipolar resulting in maximum SPL of the first BPF to be on the axis of the tube axial fan. In fact, it resembles more like the superposition of the longitudinal dipolar and lateral quadrupolar patterns. Moreover,

there is a 90° phase angle between the peaks of the numerical and experimental SPLs of the first BPF.

The maximum SPL difference between numerical and experimental results at the first BPFs happens to be at 30° position. Since FW-H equation solves the directivity of the fan as dipole, it predicts first BPF lower than experimental results on two sides of the tube axial fan while it over predicts SPL on the fan axis.

The numerical and experimental sound pressure levels and relative directivities of the tube axial fan at the second BPF are shown in Figure 41 and Figure 42, respectively.

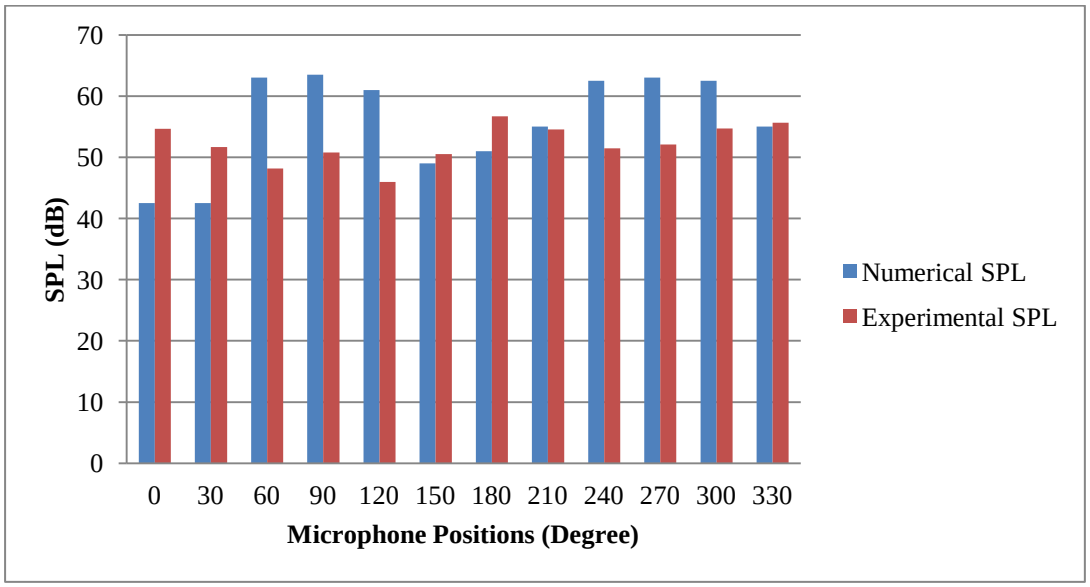

Figure 41 – Predicted and measured sound pressure levels of the tube axial fan at the second BPF

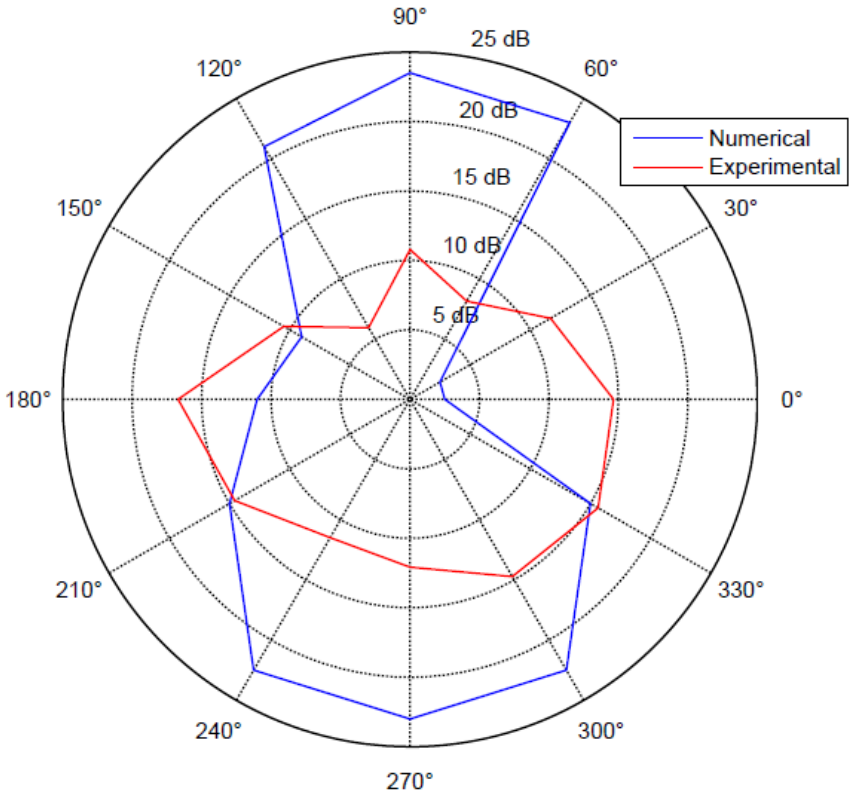

Figure 42 – Relative directivities of predicted and measured SPL of the tube axial fan at second BPF

As for the directivity of the tube axial fan at second BPF, experimental results indicate that the tube axial fan has a characteristic of a longitudinal quadrupole-like source as can be seen from Figure 42. The maximum peaks occur at the sides of the tube axial fan. However, FW-H equation predicts the characteristic of the tube axial fan at second BPF as a dipole-like emission. The maximum SPL differences between numerical and experimental results are near the tube axial fan axis. The numerical and experimental results are almost similar at near the sides of the tube axial fan at the second BPF.

Figure 43 shows the numerical and experimental sound pressure levels of the tube axial fan at the third BPF and Figure 44 indicates the numerical and experimental relative directivities of the tube axial fan at the third BPF.

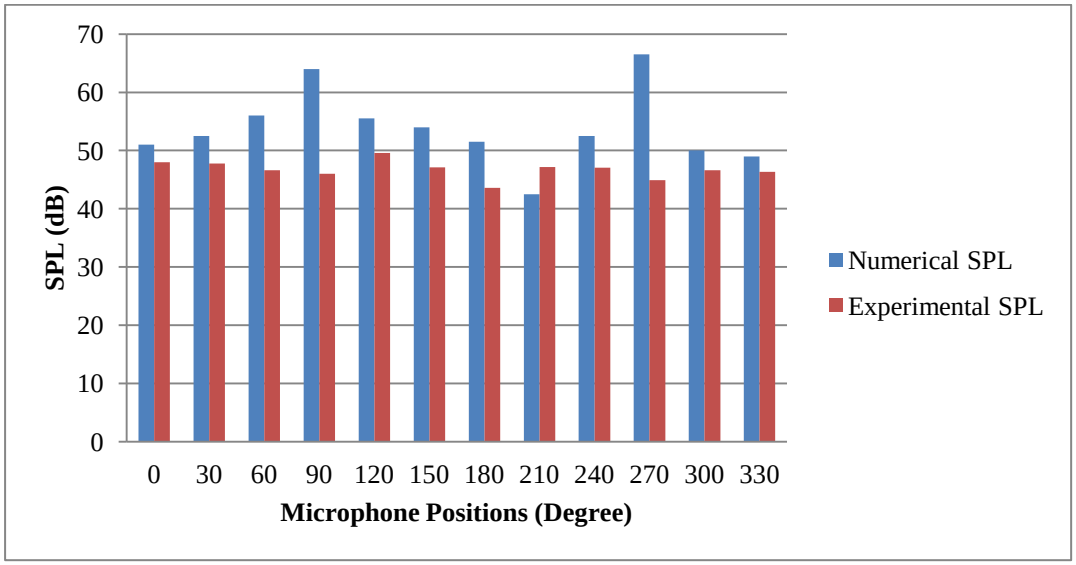

Figure 43 – Predicted and measured sound pressure levels of the tube axial fan at the third BPF

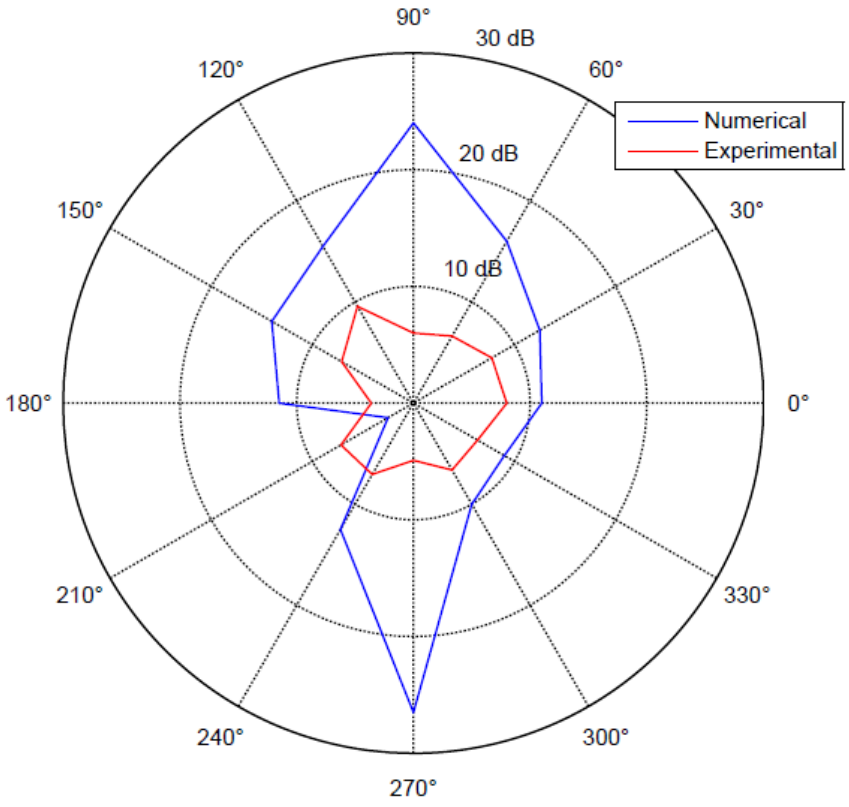

Figure 44 – Relative directivities of predicted and measured SPL of the tube axial fan at the third BPF

The tube axial fan has a characteristic of an anisotropic noise radiation at third BPF as shown in Figure 44. On the other hand, FW-H equation predicts that the tube axial fan has a dipolar-like emission at the third BPF. The maximum SPL of the third BPF was measured at the 120° position, whereas FW-H equation finds the peaks on the fan axis. The maximum SPL differences between numerical and experimental results are observed on the tube axial fan axis while the differences are less on the sides of the tube axial fan at the third BPF.

6.3.2 The Comparison of Numerical and Experimental Sound Spectrum of Tube Axial Fan at Octave Band Center Frequencies

As for the octave band center frequencies, the numerical and experimental sound pressure levels of the tube axial fan are compared for 500 Hz, 1000 Hz and 2000 Hz octave bands in Figure 45, Figure 47 and Figure 49, respectively. The predicted and measured relative directivities of the tube axial fan are indicated for 500 Hz, 1000 Hz and 2000 Hz in Figure 46, Figure 48 and Figure 50, respectively.

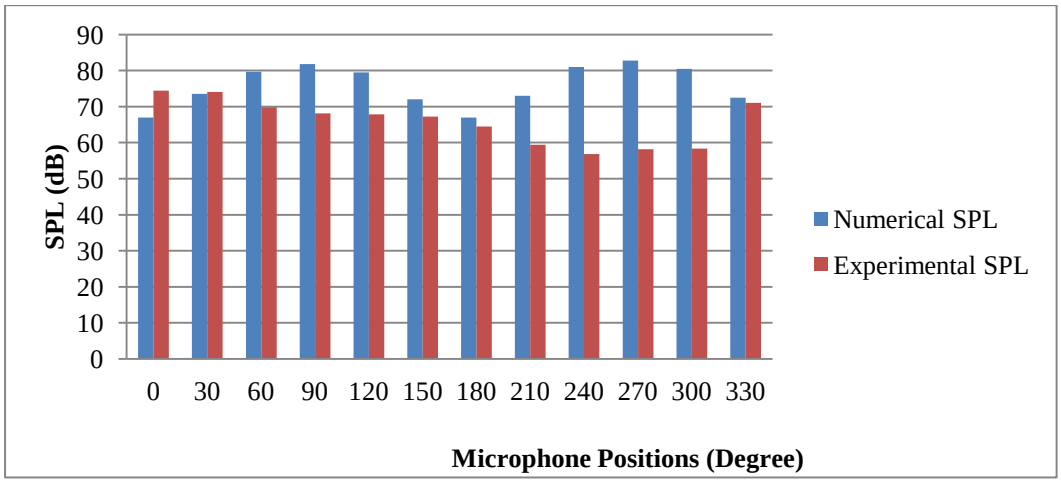

Figure 45 – Predicted and measured sound pressure levels of the tube axial fan at 500 Hz octave band

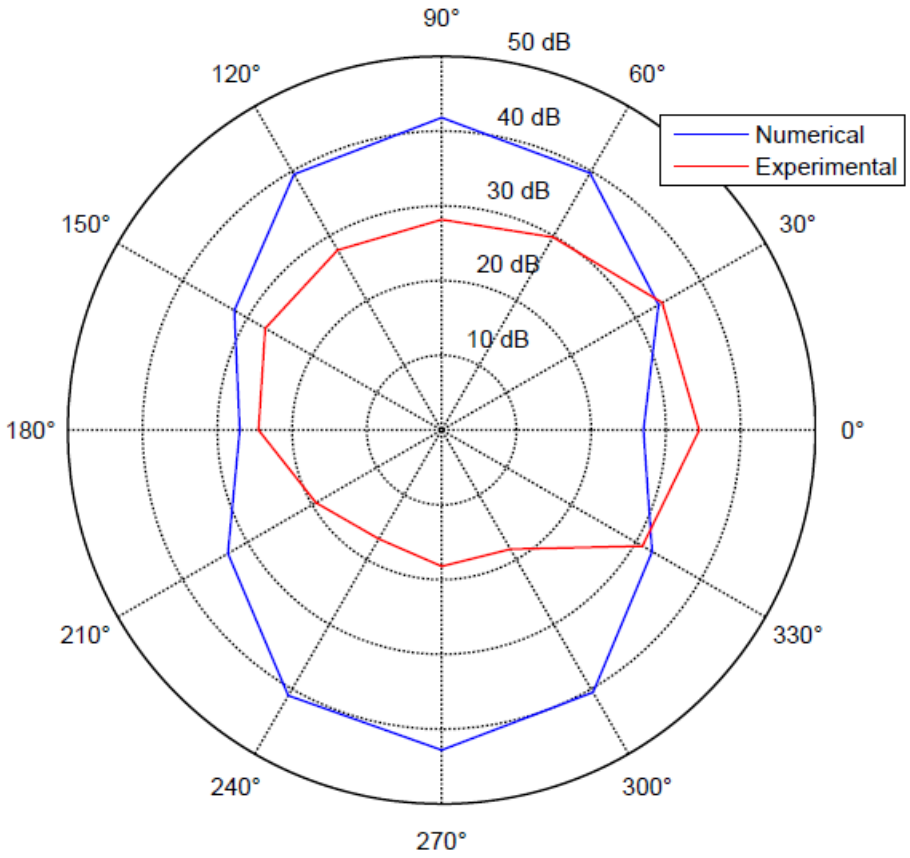

Figure 46 – Relative directivities of predicted and measured SPL of the tube axial fan at 500 Hz octave band

The directivity of the tube axial fan at 500 Hz octave band has the same characteristic as at the first BPF ground to the fact that 500 Hz octave band center frequency includes the first BPF and noise at the first BPF is the most dominant noise over the 500 Hz octave band. It is difficult to interpret the measured directivity of the tube axial fan at 500 Hz octave band in terms of dipolar-like or quadrupolar-like emission patterns. On the other hand, the numerical results indicate that the tube axial fan has a characteristic of dipolar sound source at 500 Hz octave band. The maximum SPL difference between numerical and experimental results is at 270° position. The FW-H equation gives better results at the inlet side of the tube axial fan than at the outlet side of the tube axial fan at 500 Hz octave band.

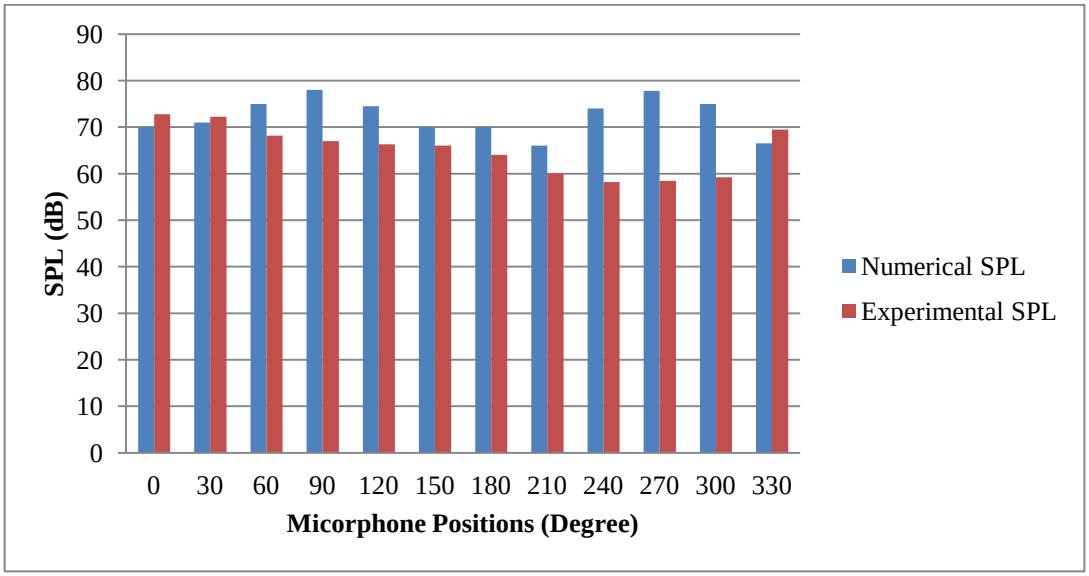

Figure 47 – Predicted and measured sound pressure levels of the tube axial fan at 1000 Hz octave band

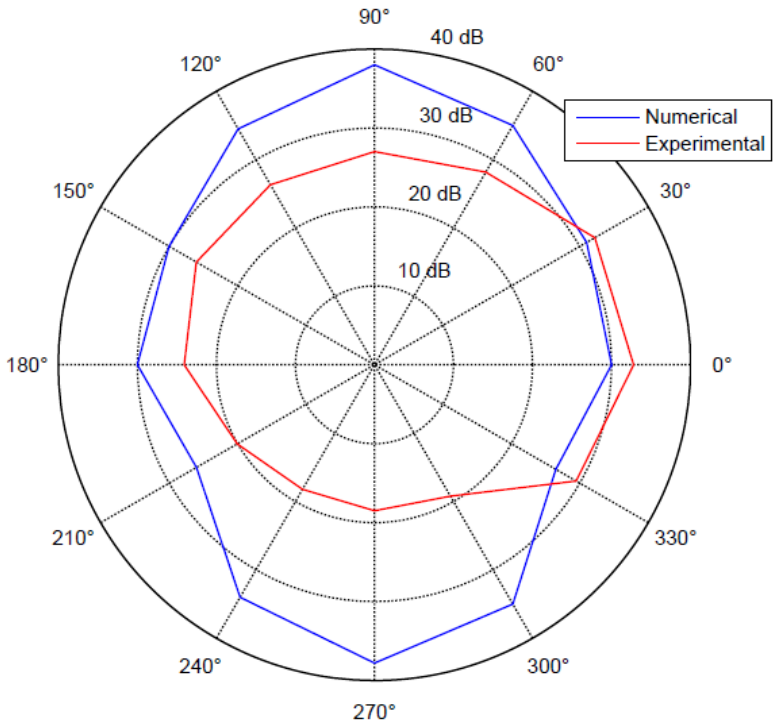

Figure 48 – Relative directivities of predicted and measured SPL of the tube axial fan at 1000 Hz octave band

The tube axial fan has almost similar directivity pattern at 1000 Hz octave band as at 500 Hz octave band. As expected, FW-H model determines the directivity pattern of the tube axial fan as dipolar. The maximum SPL was measured at 330° position whereas FW-H model predicts the maximum SPL on the fan axis, 270° position. The FW-H model predicts the fan noise at inlet side of the tube axial fan better than at outlet side of the tube axial fan.

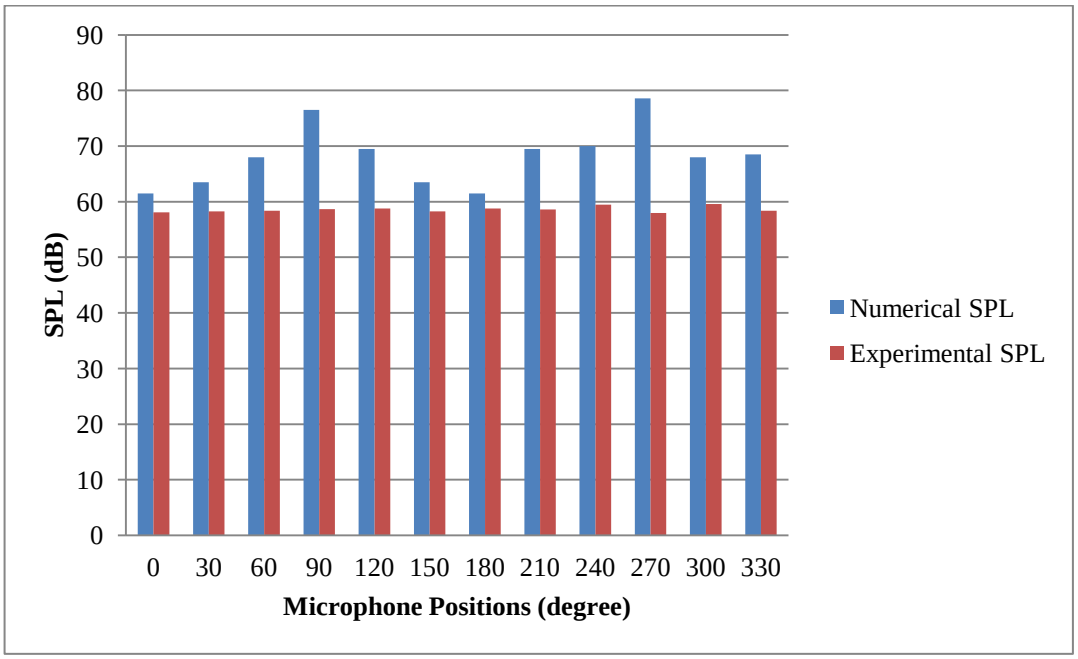

Figure 49 – Predicted and measured sound pressure levels of the tube axial fan at 2000 Hz octave band

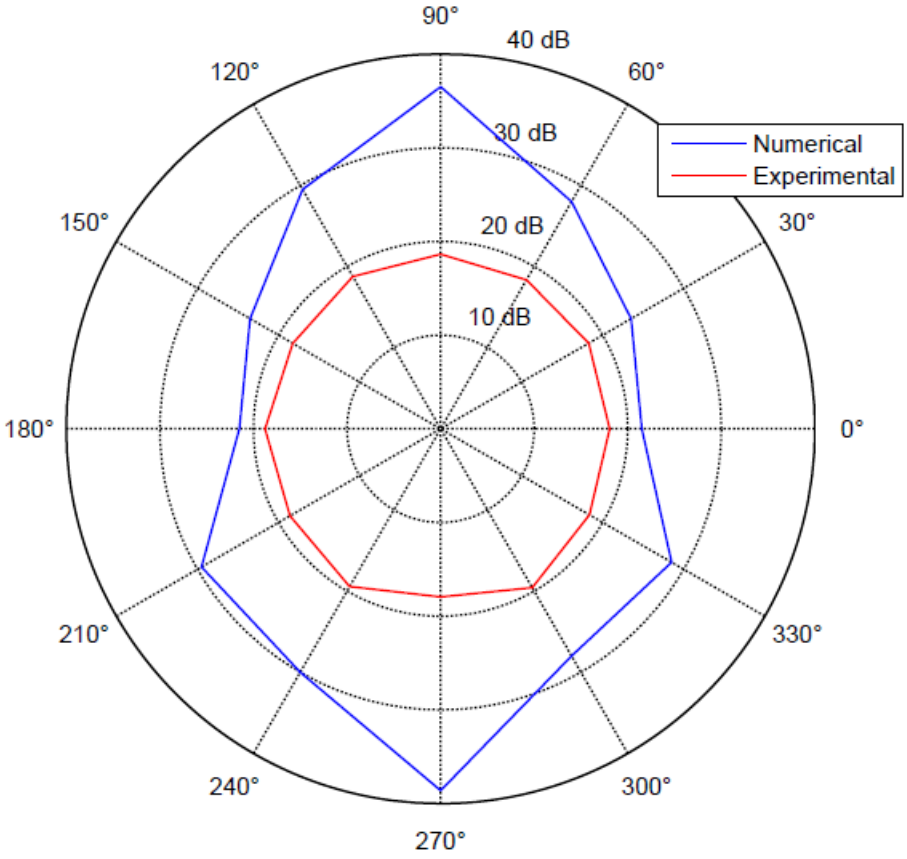

Figure 50 – Relative directivities of predicted and measured SPL of the tube axial fan at 2000 Hz octave band

The tube axial fan has an experimental characteristic of monopole-like emission pattern at 2000 Hz octave band. However, the numerical directivity of the tube axial fan is dipole. Therefore, the maximum SPL differences occur on the tube axial fan axis.

6.4 The Comparison of Experimental Noise of Tube Axial Fan and Tube Axial Fan with Blockage Plate

6.4.1 The Comparison of Experimental Sound Spectrum of Tube Axial Fan and Tube Axial Fan with Blockage Plate at the First Three BPFs

The experimental sound pressure levels of the tube axial fan and the tube axial fan with blockage plate at 0°, 90°, 180° and 270° microphone positions are compared in Figure 51, Figure 52, Figure 53 and Figure 54, respectively.

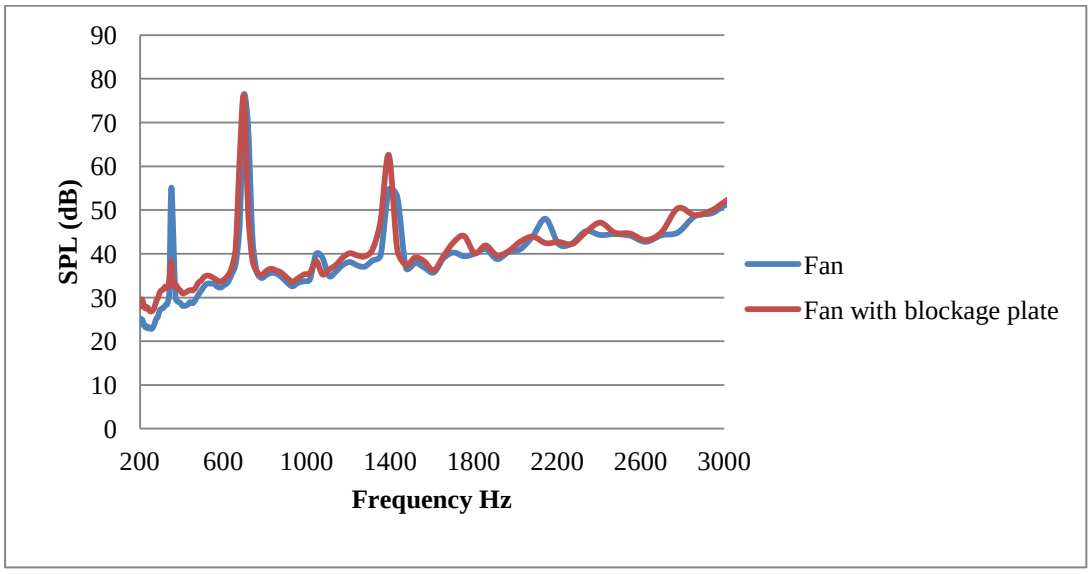

Figure 51 – Measured sound pressure levels of the tube axial fan and tube axial fan with blockage plate at 0° microphone position

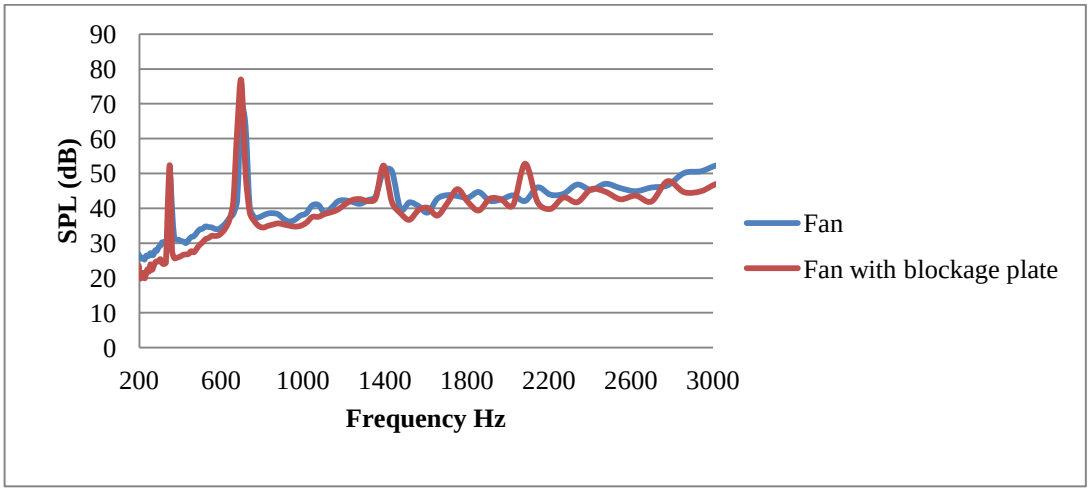

Figure 52 – Measured sound pressure levels of the tube axial fan and tube axial fan with blockage plate at 90° microphone position

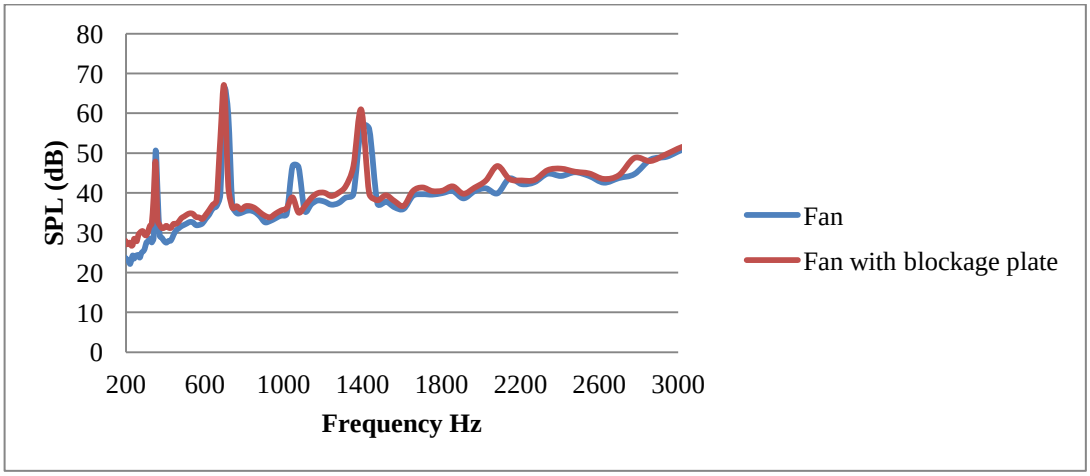

Figure 53 – Measured sound pressure levels of the tube axial fan and tube axial fan with blockage plate at 180° microphone position

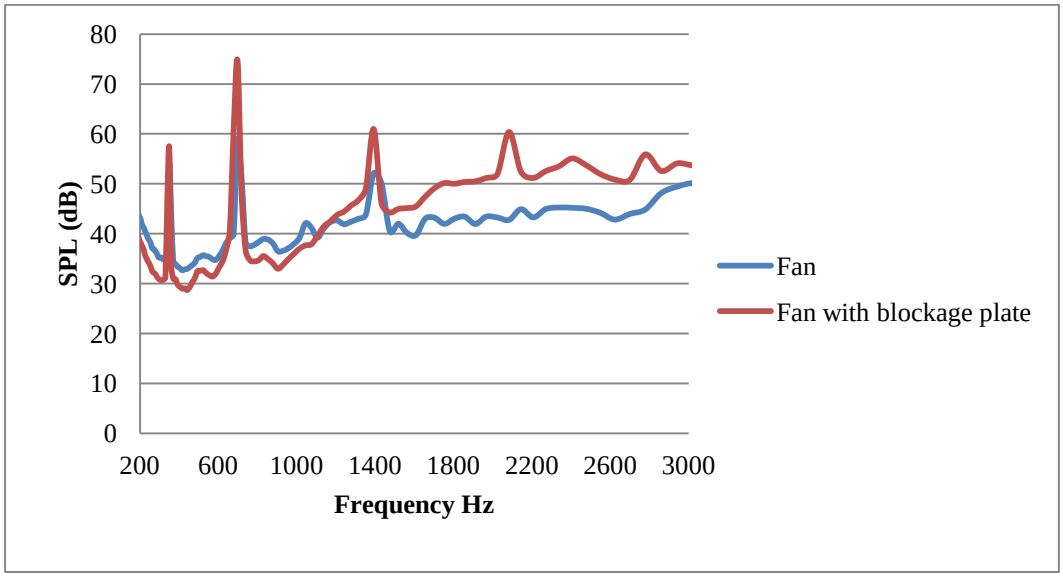

Figure 54 – Measured sound pressure levels of the tube axial fan and tube axial fan with blockage plate at 270° microphone position

The existence of the blockage plate in front of the tube axial fan causes fan noise radiation to increase on the fan axis more than on the sides of the fan. Especially, the maximum change in SPL occurs at the 270° microphone position at which both tonal and broadband components increase incredibly. The sound pressure level of the tube axial fan rises high at the outlet of the tube axial fan. A peak at the third BPF of the tube axial fan is not visible at all microphone positions since the broadband noise dominates as frequency increases. However, a peak at the third BPF becomes more visible owing to the blockage plate at all microphone positions.

The measured sound pressure levels of the tube axial fan and the tube axial fan with blockage plate at the first BPF are shown in Figure 55 and the measured relative directivities pattern of the tube axial fan and the tube axial fan with blockage plate at the first BPF are shown in Figure 56.

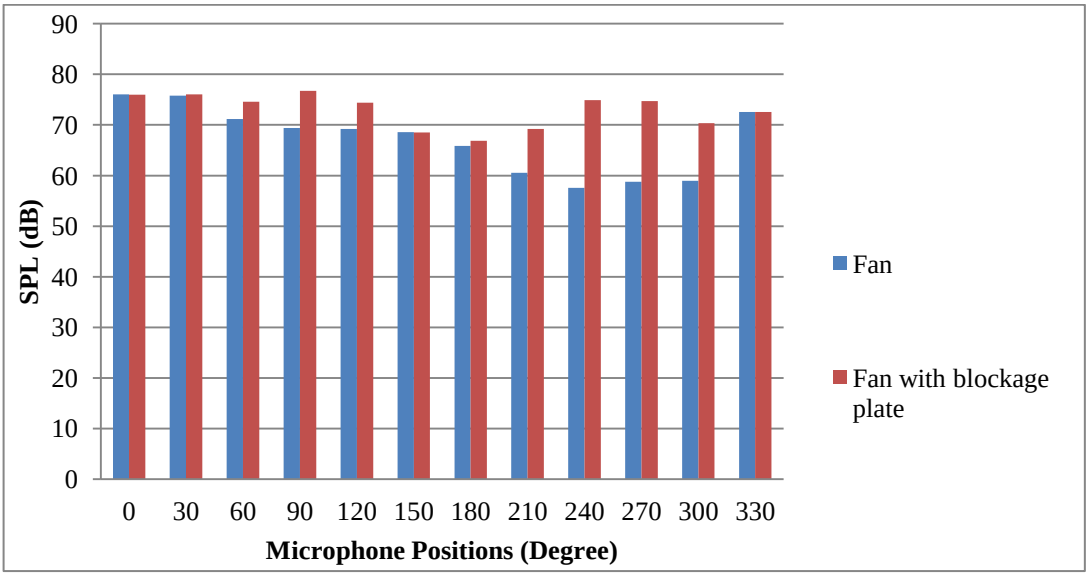

Figure 55 – Measured sound pressure levels of the tube axial fan and tube axial fan with blockage plate at the first BPF

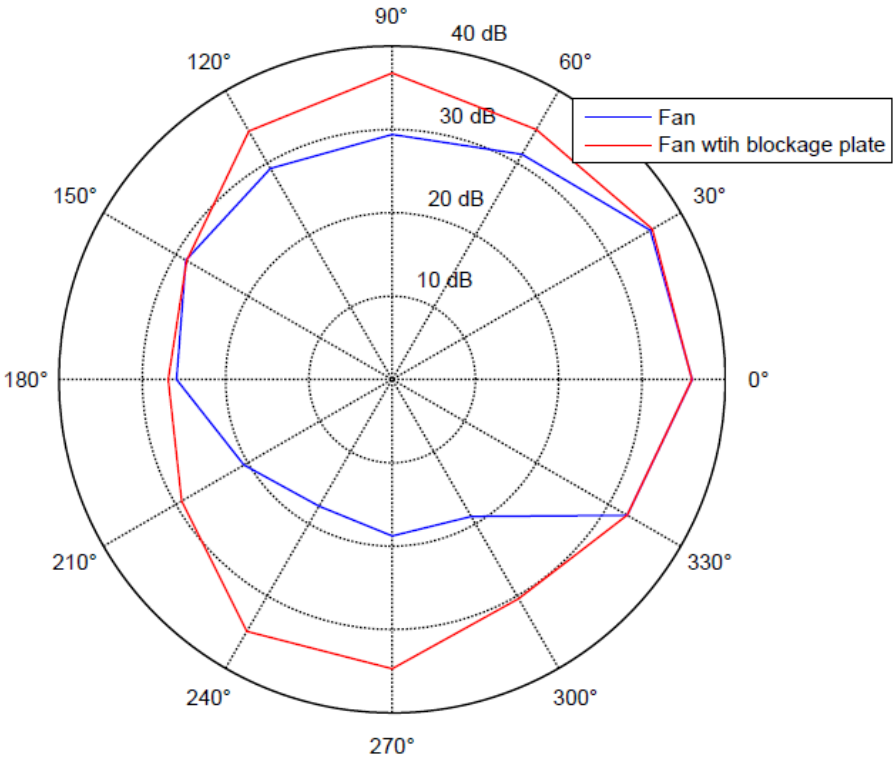

Figure 56 – Relative directivities of measured SPL of the tube axial fan and tube axial fan with blockage plate at first BPF

The presence of blockage plate mostly affects fan noise on the fan axis at the first BPF, giving rise to the directivity pattern to change into dipolar-like emission. The maximum SPL level of the tube axial fan with blockage plate at the first BPF was recorded at 90° microphone position.

The sound pressure levels and relative directivities of the tube axial fan and the tube axial fan with blockage plate at the second BPF are shown in Figure 57 and Figure 58, respectively.

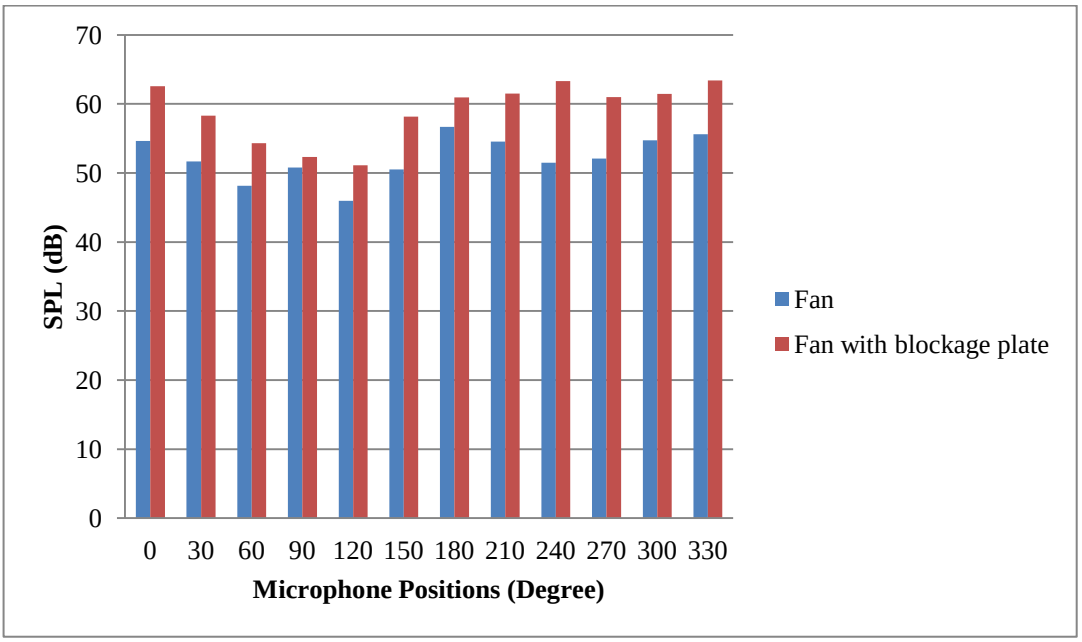

Figure 57 – Measured sound pressure levels of the tube axial fan and tube axial fan with blockage plate at the second BPF

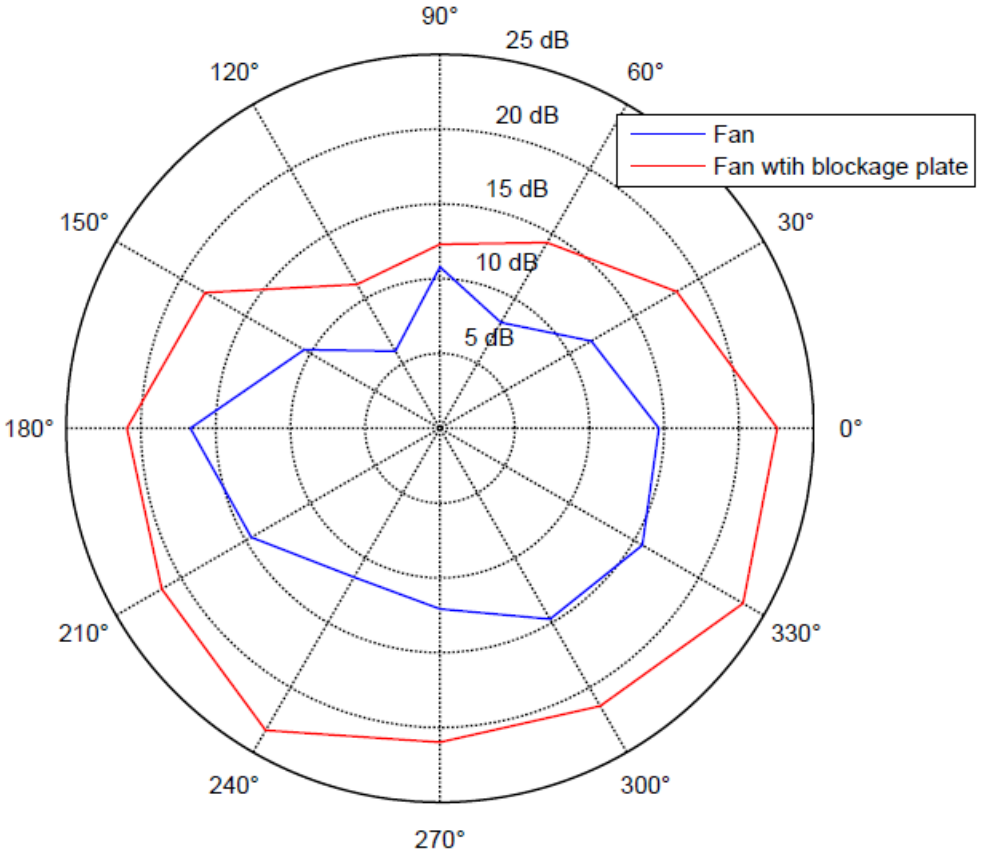

Figure 58 – Relative directivities of measured SPL of the tube axial fan and tube axial fan with blockage plate at second BPF

The blockage plate gives rise to an increase in noise levels at all microphone positions at the second BPF. However, the directivity does not lose its anisotropy this frequency. To put it differently, directivity pattern of the fan with blockage plate cannot be defined simply in terms of dipole or quadrupole sound sources at the second BPF. The fan with the blockage plate has the maximum fan noise level at 240° microphone position at the second BPF. The least affected location from the blockage plate is the 90° microphone position.

Figure 59 indicates the measured sound pressure levels of the tube axial fan and the tube axial fan with blockage plate at the third BPF and Figure 60 compares the measured relative directivities of the tube axial fan and the tube axial fan with blockage plate at the third BPF.

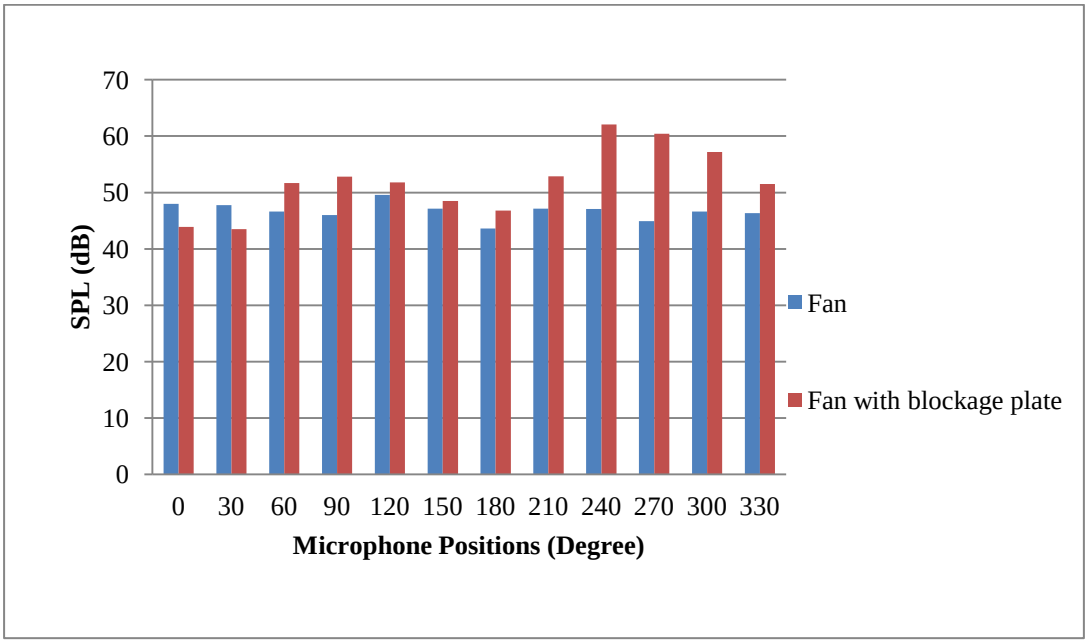

Figure 59 – Measured sound pressure levels of the tube axial fan and tube axial fan with blockage plate at the third BPF

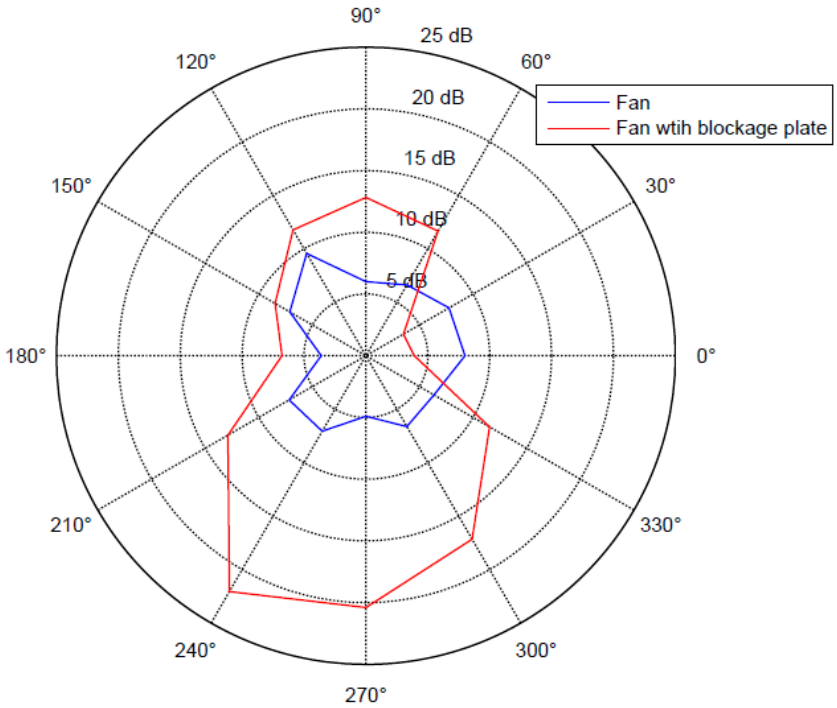

Figure 60 – Relative directivities of measured SPL of the tube axial fan and tube axial fan with blockage plate at third BPF

The fan noise decreases at the 0° and 30° microphone positions owing to the blockage plate and increases at the other microphone locations at the third BPF. The directivity of the fan alters into the dipole-like emission. The peak at the outlet side of the tube axial fan is located at the 240° microphone position. This means that the dipole characteristic of the fan with the blockage plate shifted by 30°.

6.4.2 The Comparison of Experimental Sound Spectrum of Tube Axial Fan and Tube Axial Fan with Blockage Plate at Octave Band Center Frequencies

As for the octave band center frequencies, the experimental sound pressure levels of the tube axial fan and the tube axial fan with blockage plate are compared for 500 Hz, 1000 Hz and 2000 Hz octave bands in Figure 61, Figure 63 and Figure 65, respectively. The measured relative directivities of the tube axial fan and the tube axial fan with blockage plate are shown for 500 Hz, 1000 Hz and 2000 Hz in Figure 62, Figure 64 and Figure 66, respectively.

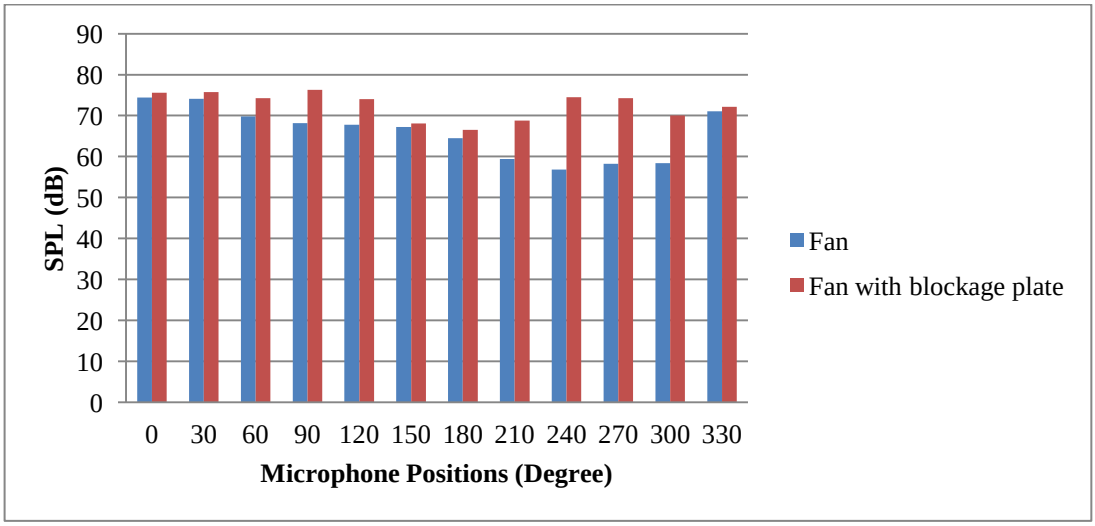

Figure 61 – Measured sound pressure levels of the tube axial fan and tube axial fan with blockage plate at 500 Hz octave band

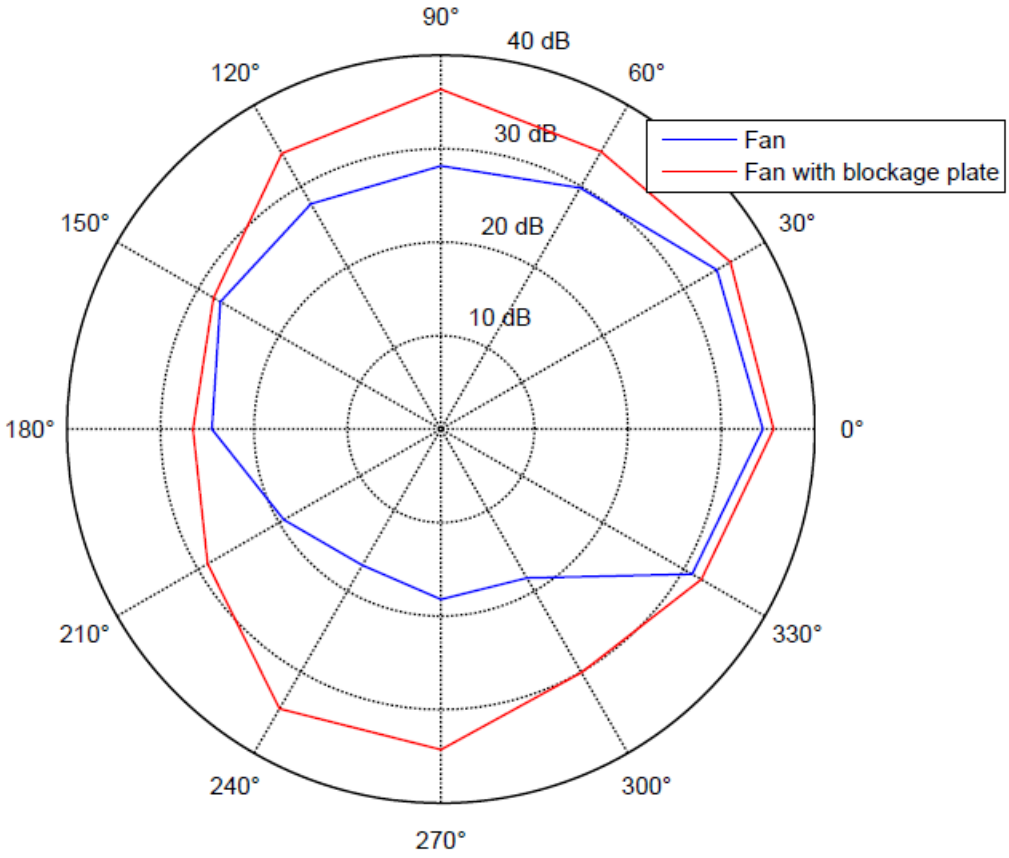

Figure 62 – Relative directivities of measured SPL of the tube axial fan and the tube axial fan with blockage plate at 500 Hz octave band

The blockage plate changes not only the magnitude of the SPL of the fan but the directivity of the fan, as well. The blockage plate changes the directivity of the fan from an anisotropy pattern to dipolar-like emission pattern at 500 Hz octave band. In fact, the dipolar pattern on the outlet side of the fan skewed by 30°. Consequently, the maximum increase in SPL due to blockage plate at 500 Hz is obtained at 240° microphone position.

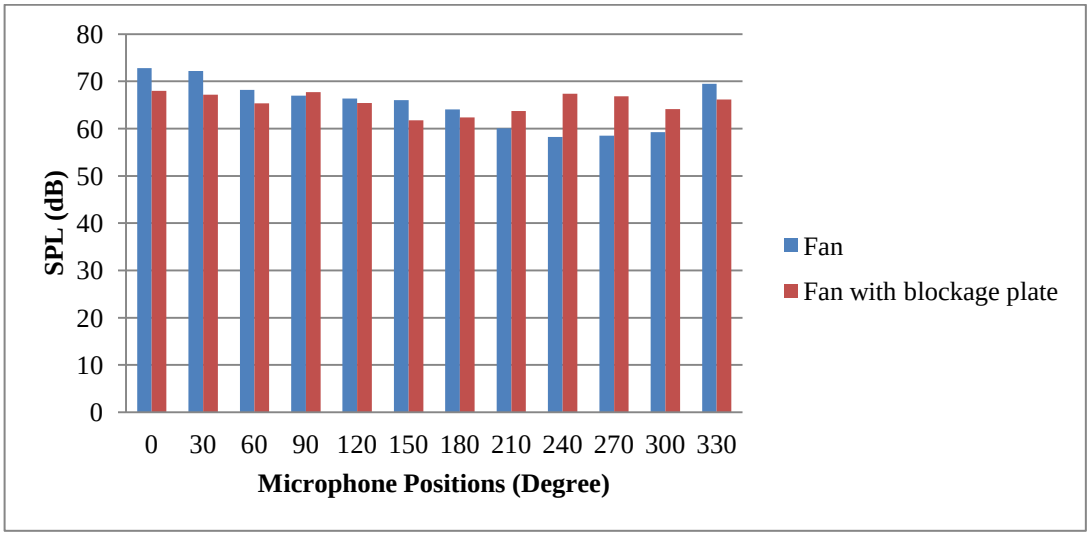

Figure 63 – Measured sound pressure levels of the tube axial fan and tube axial fan with blockage plate at 1000 Hz octave band

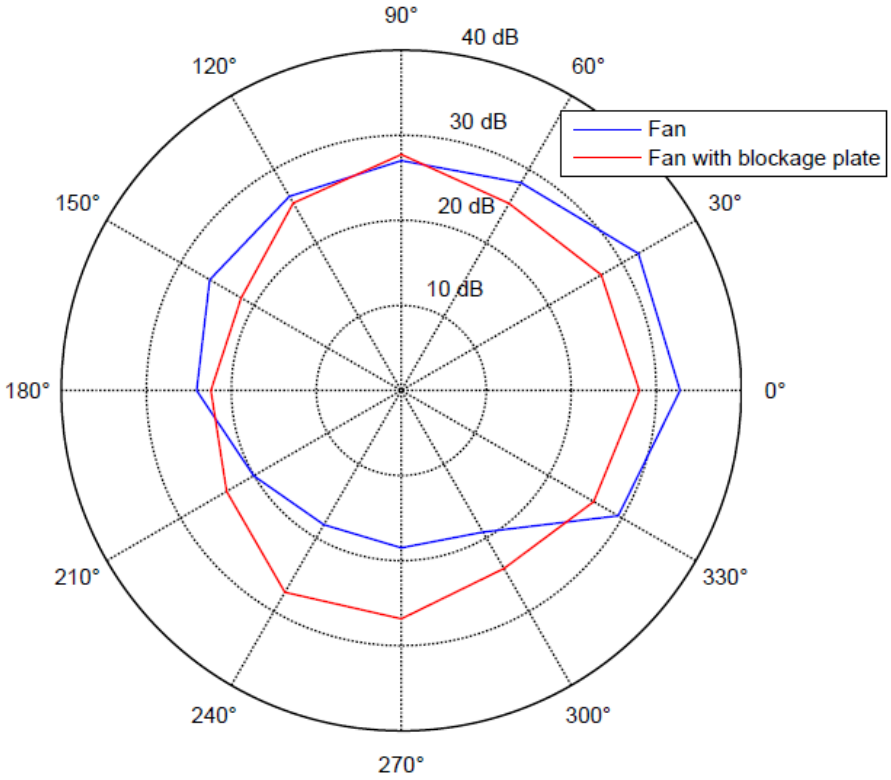

Figure 64 – Relative directivities of measured SPL of the tube axial fan and tube axial fan with blockage plate at 1000 Hz octave band

The blockage plate does not increase noise level at all microphone positions at 1000 Hz as at 500 Hz. In other words, the noise levels on the fan axis decreases while it rises on the fan axis due the blockage plate. This causes the fan to have dipolar-like emission at 1000 Hz.

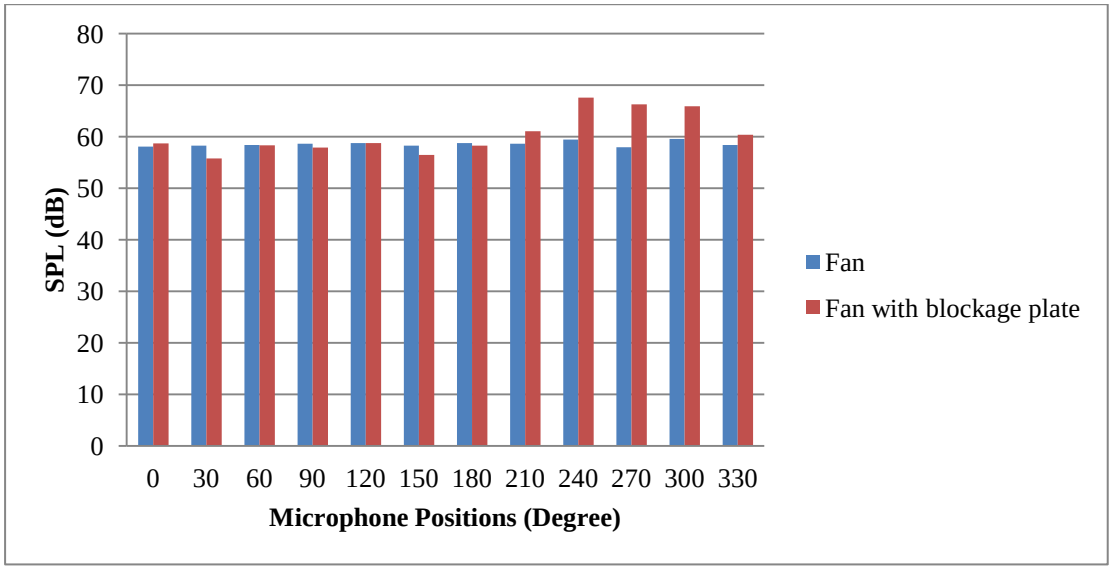

Figure 65 – Measured sound pressure levels of the tube axial fan and tube axial fan with blockage plate at 2000 Hz octave band

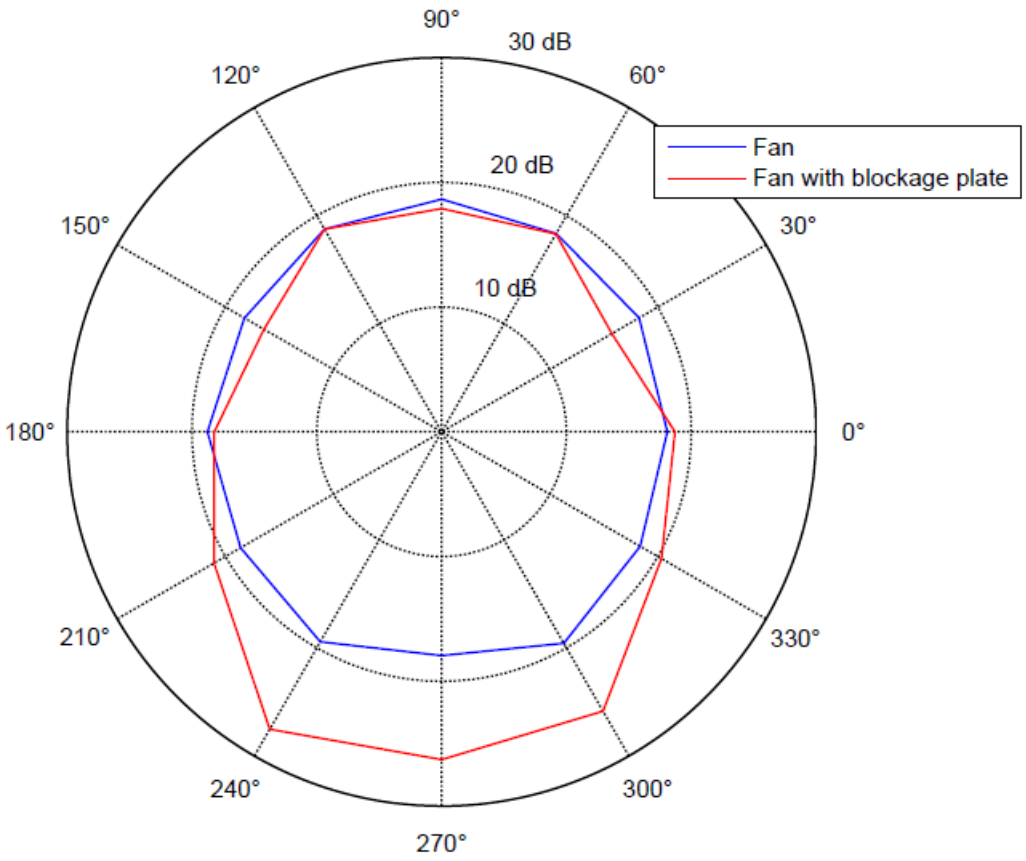

Figure 66 – Relative directivities of measured SPL of the tube axial fan and tube axial fan with blockage plate at 2000 Hz octave band

The blockage plate mostly affects the fan noise at the 240°, 270° and 300° microphone positions at 2000 Hz. Therefore, the directivity of the fan transforms from monopole-like to dipole-like sound source at 2000 Hz because of blockage plate.

CHAPTER 7

SUMMARY AND CONCLUSIONS

7.1 Summary

In this study, the tube axial fan noise has been investigated numerically and experimentally.

In the numerical study, the flow induced noise of the tube axial fan is predicted in FLUENT 14.0. The flow and acoustic solvers are coupled in FLUENT. To begin with, the transient flow is solved by applying realizable k-ε turbulence model with enhanced wall treatment. Then, acoustic data are recorded by coupling realizable k-ε turbulence model with porous FW-H equation in FLUENT. The tonal noise and noise at the interested octave band center frequencies are examined.

The experiment was carried out in a semi-anechoic room of ASELSAN A.Ş.. The sound pressure levels of the tube axial fan and the tube axial fan with blockage plate were recorded. The predicted and measured SPLs are compared and the predicted noise is in a reasonably good agreement with the measured noise data. Moreover, the noise directivity pattern of the tube axial fan is examined numerically and experimentally. The numerical directivity of the tube axial fan is found to be dipolar. On the other hand, the experimental directivity of the fan has such a directivity pattern that cannot be described simply in terms of monopole, dipole or quadrupole noise emission patterns. Furthermore, the tube axial fan with blockage plate has a dipolar-like emission pattern.

Figure 61 shows the procedures of the numerical analysis of the noise of the tube axial fan in FLUENT 14.0.

7.2 Conclusions

The noise produced by the tube axial fan is investigated by both numerically and experimentally for comparative evaluation. The numerical approach over predicts the sound pressure levels with respect to the measured sound pressure level of the fan. The predicted sound pressure levels at the first BPF and second harmonic at 12 different locations are predicted well enough. However, the differences between numerical and experimental results get larger at the third BPFs. The maximum errors at the third BPF happen to be on the axis of the tube axial fan. As for octave band center frequencies, the sound pressure levels of the tube axial fan are over predicted at 500 Hz, 1000 Hz and 2000 Hz. The maximum errors are located at the outlet side of the fan at 500 Hz whereas the maximum errors happen to be observed at the axis of the tube axial fan.

The numerical analysis over predicts the tube axial fan noise and the reasons for the differences between the numerical and experimental SPLs are that

- The fan speed is the most significant parameter affecting SPL. Sound power level of the axial fan noise showing dipole emission pattern is proportional to the sixth power of the fan speed [21]. As a consequence, a little change in the fan speed will incredibly alter the fan noise. In the experiment, the actual fan speed was likely not to be exactly 21000 rpm since the measured fan speed was oscillating between 20800 rpm and 21180 rpm values. Therefore, there is a high possibility that the experimental fan speed was lower than 21000 rpm. For this reason, the experimental results should be less than numerical results.
- Fan noise was recorded in 1/24 octave bands by the Toughbook. 1/24 octave band center frequencies do not have the same values as the first three BPF. The expected experimental first, second and third BPFs are 700 Hz, 1400 Hz and 2100, respectively. However, in the recorded data the first three BPFs are found to be 697.8 Hz, 1392.4 Hz and 2083.29 Hz, respectively. As a result, the actual peak could not been captured by 1/24 octave band due to its resolution bandwidth.

- Mesh independency has not been applied due to the limited computational power. The maximum mesh size is determined to be less than one to the sixth of the wavelength at the maximum frequency of interest.

The numerical directivity of the tube axial fan is dipole for the first three BPFs and 500 Hz, 1000 Hz and 2000 Hz octave band center frequencies. However, the experimental directivity of the fan cannot be interpreted in terms of simple dipole or quadrupole for the same frequencies except for 2000 Hz octave band center frequency at which the fan has monopole-like emission pattern. However, at low Mach number (M=0.22), dipole source is expected to dominate whereas monopole and quadrupole sources are not significant. The maximum SPL was measured at 0° microphone position at the first BPF. On the other hand, the peak experimentally occurred at 180° microphone position at the second BPF. However, the peak shifted to 120° microphone position at the third BPF. The maximum SPL was recorded at 0° microphone position for both 500 Hz and 1000 Hz octave band.

The reasons for the differences between the numerical and experimental noise characteristic of the tube axial fan are that

- The asymmetries in the tube axial fan construction may give result to forces acting on the blades to differ. Thus, different force loadings will cause anisotropic noise directivity.
- The tube axial fan motor noise might affect the directivity of the tube axial fan at low frequencies.

The tube axial fan with blockage plate has a dipolar-like emission at the first BPF, the third BPF, 500 Hz octave band, 1000 Hz octave band and 2000 Hz octave band. However, the directivity pattern of the fan with blockage plate at the second BPF cannot be defined simply in terms of dipole or quadrupole sound sources because of having anisotropy noise emission. The fan with the blockage plate has the maximum fan noise level at 240° microphone position at the second BPF. The least affected location from the blockage plate at the second BPF is the 90° microphone position.

The reasons for increases in SPL of the fan noise due to the blockage plate are that

- The blockage plate acts as a blockage for the uniform inlet flow. Hence, the unsteady loadings on the blade surfaces rise. Thus, this results in more vortex formations inside the casing of the fan giving rise to amplification of both the tonal noise and broadband noise.
- The blockage plate reflects the fan noise. The largest amount of reflection of the fan noise is located on the fan axis and the least amount of the reflection of the fan noise is on the sides of the fan. Consequently, the maximum increases in the fan noise occur on the fan axis at the outlet side of the fan.

7.3 Recommendations for Future Work

Some recommendations for future work are given below:

- The fan speed should be adjusted to 21000 rpm with the smallest speed error as much as possible by using more accurate tachometer.
- The fan noise should be recorded with narrow band sound analyzer. As a result, the frequency at which a peak occurs can be captured.
- The surfaces of the blades of tube axial fan should be meshed with hexahedral elements.
- The sound data should be recorded at least 10 full rotations of the tube axial fan in FLUENT so that the frequency resolution shall rise, which results in recording more sound data in the same interested frequency range. Thus, a more accurate comparison between BPFs of the numerical and experimental results can be done.
- LES turbulence model, reported to be the best turbulence model for axial fan noise, might be selected instead of realizable k-ε turbulence model. As an extension of this study, LES turbulence model is investigated by applying the same mesh and boundary conditions. In fact, all the parameters are the same as in the realizable k-ε turbulence model such as, time step, convergence creation, time duration for obtaining acoustical data and so on. However, the usual practice is to take 10 elements per wavelength of the

maximum frequency of interest when carrying out LES analysis [29]. The same maximum mesh size of 14 mm for LES analysis yields to a corresponding maximum frequency of interest of approximately 2450 Hz while minimum frequency of interest is the same as in realizable k-ε analysis, which is 250 Hz. Sample result of LES analysis at 150° microphone position is shown in Figure 67. Peaks at the BPF and its harmonics are well documented as illustrated in the figure though the peak level is under predicted somewhat 12 dB lower than the experimental counterpart at the BPF of 700 Hz.

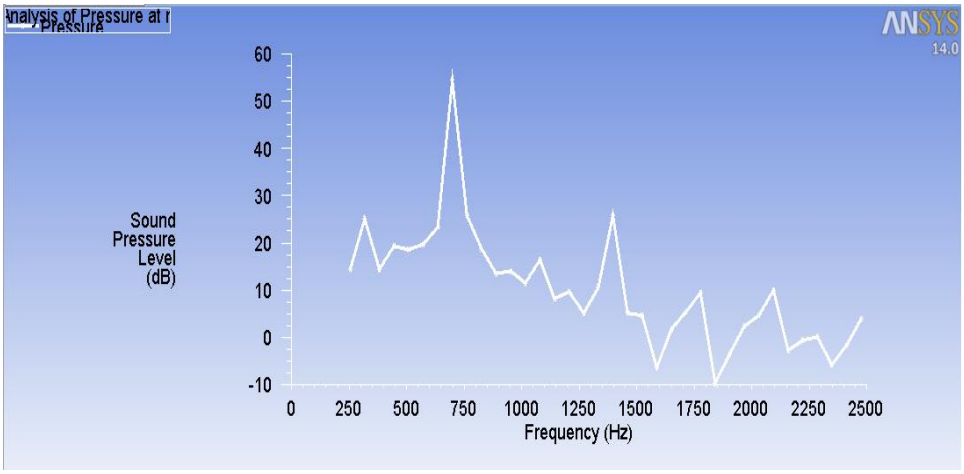

Figure 67 – Predicted sound pressure level spectrum of the fan at 150° microphone position with LES turbulence modeling

- The effects of cooling fins on tube axial fan noise can be further numerically investigated as described in this study.

REFERENCES

[1] Wook Kim, Wan-Ho Jeon, Jang-Hyung Cho, *"Numerical Study on the Noise Generation of the Axial Flow Fan in a Refrigerator"*, INTER-NOISE 2006, 2006.

[2] Gerald C. Lauchle, John R. MacGilivray and David C. Swanson, "*Active control of Axial-Flow Fan Noise*", Acoustical Society of America, January 1997.

[3] Johannes Hyrynen,*" Prediction Models Showing Effects of Design Parameters on Induction Machine Cooling Fan Performance and Sound Power"*, Inter-Noise 2002, 2002.

[4] Sheam-Chyun Lin and Chien-An Chou, "*Blockage Effect of Axial-Flow Fans Applied on Heat Sink Assembly",* Applied Thermal Engineering 24, pp. 2375-2389, 2004.

[5] Andrea Cattanei, Riccardo Ghio, Alessandro Bongiovi," *Reduction of the Tonal Noise Annoyance of Axial Flow Fans By Means of Optimal Blade Spacing*", Applied Acoustics, pp. 1323-1345, and 2007.

[6] Yoon-Shik Shin, J. Stuart Bolton, Luc G. Mongeau,*" Inflow Treatment For Small Scale Axial Fans Under Unfavorable Inflow Conditions"*, Inter-Noise 2009, 2009.

[7] S. Bianchi, A. Corsini and A. G. Sheard,*" Experimental Characterization of the Far-Field Noise in Axial Fans Fitted with Shaped Tip End-Plates"*, ISRN Mechanical Engineering, 24 January 2012.

[8] Wook Kim, Wan-Ho Jeon, Jang-Hyung Cho, *"Numerical Study on the Noise Generation of the Axial Flow Fan in a Refrigerator"*, INTER-NOISE 2006, 2006.

[9] Li Zhang, Yingzi Jin, "*Effect of Blade Numbers on Aerodynamic Performance and Noise of Small Axial Flow Fan*", Advanced Materials Research Vols. pp 796-800, 2011.

[10] Guangzhi Ren, Seung Heo, Tae-Hoon Kim and Cheolung Cheong, *"Response Surface Method-Based Optimization of the Shroud of an Axial Cooling Fan For High Performance and Low Noise*" Journal of Mechanical Science and Technology 27 (1) (2013) 33~42

[11] Li Zhang and Yingzi Jin, "*Numerical Investigation on Vortex Structure and Aerodynamic Noise Performance of Small Axial Flow Fan*", Open Journal of Fluid Dynamics, pp. 359-367, 2012.

[12] Pal Pandian and Arun Raj, "*Flow Noise Investigation for an Unsteady Flow Past a Circular Cylinder*", International Journal of Research in Aeronautical and Mechanical Enginering, pp. 84-91, January 2014.

[13] Esra Sorgüven, Franco Magagnato and Martin Gabi," *Acoustic Prediction of a Cylinder and Airfoil Configuration at High Reynolds Number with LES and FWH*", Karlsruhe University.

[14] M. Abom and H. Boden, "*A Note on the Aeroacoustic Source Character of In-Duct Axial Fans*", Journal of Sound and Vibration, 589-598, 1995.

[15] Esra Sorguven, Yılmaz Dogan, Faruk Bayraktar and Kenan Y. Sanliturk, "*Noise Prediction via Large Eddy Simulation: Application to Radial Fans*", Noise Control Engineering Journal, 169-178, May 2009.

[16] Feng Gue, Cheolung and Taehoon Kim," *Development of Low Noise Axial Cooling Fans in a Household Refrigerator*", Journal of Mechanical Science and Technology, 2995-3004, 2011.

[17] K.M. Argüelles Diaz, J.M. Fernandez Oro, C. Santolaria and P. Fernandez Coto," *Numerical Study of the Discrete Frequency Noise Generation in an Axial Flow Fan*", University of Oviedo, Spain, 45-56,1992.

[18] Elias Tannoury, Sofiane Khelladi, Bruno Demory, Manuel Henner and Farid Bakir," *Tonal Noise Prediction of an Automotive Engine Cooling Fan: Comparison Between Analytical Models and Acoustic Analogy Results*", Journal of Mechanics Engineering and Automation, 455-463, 2012.

[19] Neise, W.," *Review of Fan Noise Generation Mechanisms and Control Methods*", Fan Noise Symposium, CETIM, France, 45-56, 1992.

[20] Gerald C. Lauchle, John R. MacGilivray and David C. Swanson, "Active *Control of Axial Fan Noise*", Acoustical Society of America, 1997.

[21] Jack E. Marte and Donald W. Kurtz, "*A Review of Aerodynamic Noise from Propellers, Rotors, and Lift Fans*", California Institute of Technology Pasadena, California, January 1, 1970.

[22] Anthony Gérard, Alain Berry, Patrice Masson," *Control of Tonal Noise From Axial Fan. Part 1: Reconstruction of Aero Acoustic Sources From Far-Field Sound Pressure*", Journal of Sound and Vibration, Volume 288,pp. 1049-1075, 20 December 2005.

[23] M.S. Howe," *Acoustics of Fluid-Structure Interactions*", Cambridge University Press, pp. 2-11 and 101-112, 1998.

[24] ANSYS FLUENT Theory Guide, ANSYS Inc., November 2011.

[25] Walter Frei,"*Which Turbulence Model should I choose for my CFD Application*" Comsol.org, September 16, 2013.

[26] Mehmet Haluk Aksel," *Notes on Fluid Mechanics*", Middle East Technical University, Volume 2, pp. 899-900 and 939-951, February 2010.

[27] Teresa S. Miller," *Turbulent Boundary Layer Models for Acoustics Analysis*", University of Texas at Austin, 2011.

[28] ISO-3744, "*Acoustics – Determination of Sound Power Levels and Sound Energy Levels of Noise Sources Using Sound Pressure – Engineering Methods for an Essentially Free Field Over a Reflecting Plane*", 2010.

[29] T. Lodygowskı and W. Sumelka," *Limitations in Application of Finite Element Method in Acoustic Numerical Simulation*", Journal of Theoretical and Applied Mechanics, pp. 849-865, 2006.

[30] D. Saatchi, M. Fathali and A. R. Khojasteh," *The Impact of Reynolds Number on the Accuracy of Two Different Turbulence Models for Acoustic Results of an Airfoil*", International Society of Acoustics and Vibration, December 25, 2006.

[31] S. Marburg," *Six Boundary Elements per Wavelength: is that Enough?*", Journal of Computational Acoustics, Vol. 10, pp. 25-51, 2002.